Biomedical Physics & Engineering
Express

ENDORSED BY
IPEM Institute of Physics and Engineering in Medicine

ACCEPTED MANUSCRIPT

Inherent error estimates for noisy-data discrimination and filter-specification in universal back-projection based photo-acoustic tomography

To cite this article before publication: Prabodh Kumar Pandey *et al* 2018 *Biomed. Phys. Eng. Express* in press https://doi.org/10.1088/2057-1976/aab5df

Inherent error estimates for noisy-data discrimination and filter-specification in universal back-projection based photo-acoustic tomography

Prabodh Kumar Pandey[1]

[1]Department of Physics, Indian Institute of Technology, Kanpur, India, 208016

E-mail: prabodh@iitk.ac.in

Naren Naik[2,3]

[2]Department of Electrical Engineering , Indian Institute of Technology, Kanpur, India, 208016

[3]Center for Lasers and Photonics , Indian Institute of Technology, Kanpur, India, 208016

E-mail: nnaik@iitk.ac.in

Prabhat Munshi[4,5]

[4]Department of Mechanical Engineering , Indian Institute of Technology, Kanpur, India, 208016

[5]Nuclear Engineering and Technology Programme , Indian Institute of Technology, Kanpur, India, 208016

E-mail: pmunshi@iitk.ac.in

Asima Pradhan[1,3]

[1]Department of Physics , Indian Institute of Technology, Kanpur, India, 208016

[3]Center for Lasers and Photonics , Indian Institute of Technology, Kanpur, India, 208016

E-mail: asima@iitk.ac.in

Abstract. Characterization of inherent reconstruction errors arising from algorithm-parameter choices is becoming an important requirement for photo-acoustic (PA) tomographic systems. In the present work, we derive an estimate of the inherent errors which arise in universal back-projection based photo-acoustic tomography (PAT) because of the filtering of the forward PA data. Based on the developed error estimates, we further devise an algorithm to choose the forward data with the best SNR from the sets of data procured under different conditions. A prudent choice of the cut-off frequency is critical to obtain good reconstructions from a forward data set. While a high cut-off frequency brings in noise artifacts in the reconstructions, a low cut-off frequency leads to loss of the features encoded in the higher frequency components. Therefore, we further propose a method to obtain an appropriate cut-off frequency, which suppresses the noise while preserving the important features in the

PA reconstruction. Numerical validations of the proposed schemes are presented for Hamming filter based smoothed UBP reconstructions of sharply varying initial pressure distributions.

PACS numbers: 42.30.Wb, 87.57.C-, 87.57.N-, 87.57.Q-

Keywords: Photo-acoustic tomography, Universal back-projection algorithm, Inherent errors, Noisy data discrimination, Optimal reconstructions

Submitted to: *Biomedical Physics & Engineering Express*

1. Introduction

When a laser pulse is incident on a sample, absorption of optical energy leads to local heating. Consequently thermo-elastic expansion takes place generating photo-acoustic (PA) waves that propagate in the medium. The photo-acoustic (PA) source, proportional to the absorbed optical energy in the sample creates an initial distribution of pressure [1]. Reconstruction of this PA source is done through photo-acoustic tomography (PAT) (also known as opto-acoustic tomography) from the boundary pressure signals captured by ultrasonic transducers on a detector grid, which partially or completely encases the specimen of interest. PAT combines the contrast and resolution advantages of optical and ultrasound interrogations respectively and hence it has immense potential in the field of biomedical imaging [2, 3, 4, 5, 6, 7]. Currently, PAT systems are being clinically tested [8]. The linear PA reconstruction problem (assuming known acoustic parameters of the medium) can be solved in several ways such as back-projection based scheme [1, 9, 10], time reversal scheme [11, 12, 13] and model-based schemes [14, 15, 16]. Typically PAT systems utilize piezoelectric transducers arrays or contact based Fabry-Perot etalons in planar [17, 18, 19, 20, 21], spherical [22, 23] and circular scanning/cylindrical [24, 25, 26] detection geometries for data acquisition.

Reconstruction accuracy is affected by many factors such as a low-pass/ band-pass filter used to ameliorate noise effects [27, 28, 29], detector bandwidth [30, 31, 32], acoustic attenuation related bandwidth truncation [27], limited-view effects [33], inhomogeneous sound speed [27, 34], finite detector aperture [30, 35] and acoustic reflections [36]. While effects such as, unknown acoustic attenuation, limited-view effects, inhomogeneous sound speed can be addressed using model-based schemes, we note that the effects such as source and detector bandwidth and acoustic-attenuation related frequency domain truncation can be modeled as low-pass/band-pass filtering operations [27, 30]. Reconstruction algorithms need to correct for these effects via deconvolution (for instance as shown in [27]); these corrections however have the effects of enhancing noisy components of the data which then needs to be addressed. Reconstruction algorithm-design corresponding to noisy data with known frequency domain truncations is thus an important aspect.

A critical aspect of setting up a practical system is thus a characterization of the reconstruction obtained with respect to the forward data. For instance, it is important to know the nature of data used to obtain the reconstruction and whether the reconstruction has been optimized with respect to various algorithmic parameters. In time reversal based PAT, an error estimate was provided with respect to the cut-off time under the non-trapping sound speed condition [13]. The choice of various parameters required in a reconstruction algorithm brings in errors inherent to the algorithm itself. With the ultimate aim of being able to design an appropriate analytical reconstruction scheme for given data-acquisition settings with corresponding frequency domain effects, our present work proposes a characterization of the inherent errors of the PA reconstruction obtained from time domain PAT using universal back-projection (UBP) algorithm, a commonly used reconstruction algorithm for PAT. The inherent error arises due to using of smoothing filters meant to ameliorate the effects of noise in the data. In our work we use a bank of filters to propose both, a scheme to distinguish between data of different noise levels, as well as an appropriate choice of filter cut-off frequency that plays a defining role in UBP algorithm. The presented scheme and results obtained are essential baseline studies towards reconstruction design corresponding to noisy data with known frequency domain truncations.

The UBP algorithm has a generic similarity to the filtered (or convolution) back-projection(FBP or CBP) algorithm [37, 38] commonly used in straight path computerized tomography (CT). Inherent error estimates have been developed for the FBP algorithm in two dimensions by Munshi et al. [39], Wells et al. [40] and Jain et al.[41] (in three dimensions). These estimates have been shown to provide information pertaining to the spatial frequency content of the phantoms and investigate instrumental errors as well as incompleteness of projection data [41, 42]. In 2014, Shakya et al. utilized these estimates in X-ray tomographic reconstructions of a three-phase flow system[43]. They implemented these estimates to verify the goodness of the projection data and quantify the X-ray absorption content of the cross-section. They further utilized the error estimates in the study of the distribution of different phase fractions in a three-phase bubble column reactor [44] and found the estimates to provide information about the size of bubbles and the attenuation of X-rays.

The band-limitedness of the detection system is responsible for the loss of a part of information about the original PA source, that is encoded in the high frequency components of the PA signals. Hence, in our error estimate calculations, the band-limited rectangular window (7) reconstruction in a given frequency window has been chosen as the datum reference. In an earlier work [28], we had presented and validated error estimates for planar detection geometry. Preliminary results of our present work for arbitrary detection geometry and noisy-data discrimination have been given in [29]. In the present work, we develop the error estimates for the UBP algorithm for an arbitrary detection geometry and propose a scheme for discriminating between data of differing noise levels. In addition, we also suggest a method to obtain an appropriate cut-off frequency to be used in the filter to obtain best possible reconstructions for a given

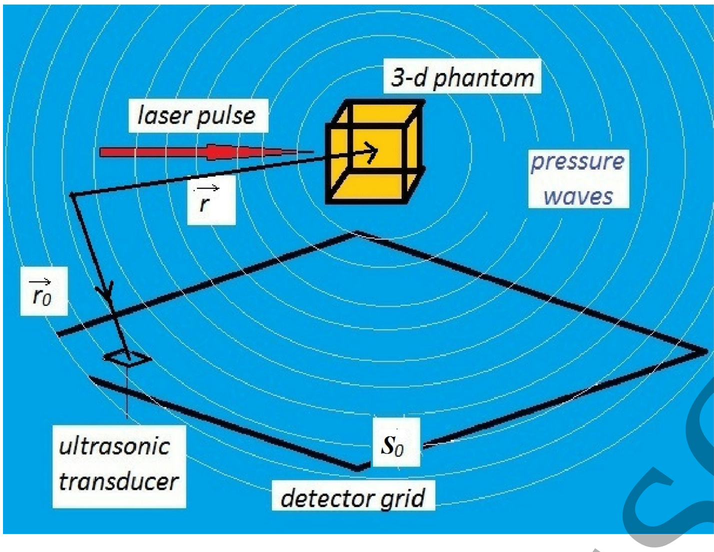

Figure 1: Detection geometry

data set. Thus, in summary, the contributions of the present work are **1)** proposing and deriving the inherent error estimates for UBP based PAT, **2)** using these error estimates to choose data with the best SNR and **3)** obtaining an appropriate cut-off frequency, which results in removal of noise significantly, while preserving the important features of the phantom. In order to validate our proposed scheme, we have presented detailed numerical studies with phantoms of differing absorber sizes and data noise levels in generic spherical and planar detection geometries.

In this paper, the inherent error estimation problem for UBP based PAT is set-up in section 2 . In section 3 the error estimate for UBP based PAT reconstruction is derived for arbitrary detection geometries. Schemes for noisy data discrimination and choosing an appropriate cut-off frequency is proposed in section 4. In section 5, we numerically validate the propositions made in sections 3 and 4. The work is summarized in section 6.

2. The inherent error estimation problem

Excitation of a sample by a $\delta(t)$ laser pulse leads to a pressure source $p_0(\vec{r}) = A(\vec{r})\Gamma(\vec{r})$ (known as PA source), where $A(\vec{r})$ is absorbed energy per unit volume, $\Gamma(\vec{r})(= v^2\beta/C_p)$ is the Gruneisen parameter, v is speed of sound, β is volumetric thermal expansion coefficient and C_p is specific heat capacity at constant pressure. Equation (1) is the PA equation (PAE) [9], which describes the propagation of PA waves in acoustically homogeneous and non-attenuating acoustic media for delta pulse excitation.

$$\left(\nabla^2 - \frac{1}{v^2}\frac{\partial^2}{\partial t^2}\right)p(\vec{r},t) = -\frac{p_0(\vec{r})}{v^2}\frac{d\delta(t)}{dt}. \tag{1}$$

The propagating PA signals are acquired using ultrasonic transducers (position vector

$\vec{r}_0$) forming a detector grid S_0 (figure 1) that completely or partially encloses the region of interest.

The inverse problem of PAT is to recover the initial PA source $p_0(\vec{r})$ from a set of boundary PA data $p(\vec{r}_0, t)$ or its Fourier transform (on variable $\bar{t} = vt$) $\tilde{p}(\vec{r}_0, k)$. In the UBP algorithm [9, 30], in order to reconstruct the PA source (p_0), back-projection term $b\left(\vec{r}_0, t = \frac{|\vec{r}-\vec{r}_0|}{v}\right)$ corresponding to each detector point $\vec{r}_0$ is evaluated and then integrated across solid angles to compute $p_0^{rec}(\vec{r})$ as:

$$p_0^{rec}(\vec{r}) = \int_{\Omega_0} b(\vec{r}_0, t = \frac{|\vec{r}-\vec{r}_0|}{v}) \frac{d\Omega_0}{\Omega_0}, \tag{2}$$

where Ω_0 is the solid angle subtended by the detector grid on the point of reconstruction ,

$$b(\vec{r}_0, t) = 2p'(\vec{r}_0, t) - 2t\frac{\partial p'(\vec{r}_0, t)}{\partial t}. \tag{3}$$

Due to filtering of the detected signal in the temporal frequency domain by a filter, characterized by function $H(k)$, the filtered signal is given by [30]

$$\tilde{p}'(\vec{r}_0, k) = H(k)\tilde{p}(\vec{r}_0, k) \tag{4}$$

and the filtered signal in time domain is given as

$$p'(\vec{r}_0, t) = \hat{\mathcal{F}}^{-1}[\tilde{p}'(\vec{r}_0, k)] = \int_{-\infty}^{\infty} p(\vec{r}_0, t')\mathcal{H}(t - t')dt', \tag{5}$$

where the operator $\hat{\mathcal{F}}^{-1}$ implies the inverse Fourier transform (IFT) and $\mathcal{H}$ is the IFT of $H(k)$. In practice, band-limited filter functions are considered for smoothening of signals. These filters are typically of the form:

$$H(k) = \begin{cases} W(k/k_c) & : |k| < k_c \\ 0 & : otherwise \end{cases}, \tag{6}$$

where $W(k/k_c)$ is a window function and k_c is the cut off frequency. Consider a band-limited rectangular window (RW) filter function, characterized by cut-off frequency k_c of the form:

$$H_{RW}(k) = \begin{cases} 1 & : |k| < k_c \\ 0 & : otherwise. \end{cases} \tag{7}$$

The filtered signal is fed into a reconstruction scheme (characterized by an operator $\hat{\mathcal{R}}$) to obtain the initial PA source

$$p_{0_W}^{rec}(\vec{r}) = \hat{\mathcal{R}}[H(k)\tilde{p}(\vec{r}_0, k))]. \tag{8}$$

For the case of noiseless data and a chosen cut-off frequency, the PA data with rectangular window filtering leads to the best reconstruction.

$$p_{0_{RW}}^{rec}(\vec{r}) = \hat{\mathcal{R}}[H_{RW}(k)\tilde{p}(\vec{r}_0, k))] \tag{9}$$

We define the inherent error in the PA reconstruction as the average error in reconstruction, considering the RW reconstruction as reference.

$$\bar{\epsilon} = \frac{1}{N}\sum_{i=1}^{N}(p_{0_W}^{rec}(\vec{r_i}) - p_{0_{RW}}^{rec}(\vec{r_i})), \tag{10}$$

where the $\vec{r_i}$ represent the locations of the points of reconstruction (indexed by i) and N is the total number of such points lying in the domain of reconstruction.

3. Inherent error estimates

In this section, we derive inherent error estimates for arbitrary detection geometries, thus generalizing our earlier results in [28]. Accuracy of PA tomographic reconstruction depends on the number of detectors, their locations, the sampling frequency of data acquisition, noise level, reconstruction algorithm and the parameters chosen in the algorithm for reconstruction. Y. Hristova has provided error estimates for the time reversal based reconstruction as a function of cut-off time [13]. The accuracy of the UBP algorithm based PAT reconstruction is dictated by the properties of the filter used, i.e. the choice of window function and the cut-off frequency. Filtering of forward signal is required to give a higher weightage to low frequency amplitudes and attenuate noisy high frequency components. The frequency domain PA equation is the Helmholtz equation written as

$$(\nabla^2 + k^2)p(\vec{r}, k) = i\frac{k}{v}p_0(\vec{r}). \tag{11}$$

The UBP algorithm is a simplified form of Green's third identity[45], according to which, the PA pressure $\tilde{p}(\vec{r}, k)$ in the region enclosed by the detection surface S_0 can be calculated [9] as

$$\tilde{p}(\vec{r}, k) = \int_{S_0} dS_0\tilde{p}(\vec{r}_0, k)[\hat{n}_0^{S_0}.\vec{\nabla}_0\tilde{G}_k^{(D)}(\vec{r}, \vec{r}_0)], \tag{12}$$

where $\hat{n}_0^{S_0}$ denotes the unit normal vector of S_0 and $\tilde{G}_k^{(D)}(\vec{r}, \vec{r}_0)$ is the Green's function corresponding to the Helmholtz equation

$$(\nabla^2 + k^2)\tilde{G}_k^{(D)}(\vec{r}, \vec{r}_0) = -\delta(\vec{r} - \vec{r}_0). \tag{13}$$

Taking the inverse Fourier transform of (12), we get

$$p(\vec{r}, \bar{t}) = \frac{1}{2\pi}\int_{-\infty}^{\infty} dk e^{ik\bar{t}} \int_{S_0} dS_0\tilde{p}(\vec{r}_0, k)[\hat{n}_0^{S_0}.\vec{\nabla}_0\tilde{G}_k^{(D)}(\vec{r}, \vec{r}_0)]. \tag{14}$$

The initial pressure source that we aim to reconstruct is $p_0(\vec{r}) = p(\vec{r}, \bar{t} = 0)$, so

$$p_0(\vec{r}) = \frac{1}{2\pi}\int_{-\infty}^{\infty} dk \int_{S_0} dS_0\tilde{p}(\vec{r}_0, k)[\hat{n}_0^{S_0}.\vec{\nabla}_0\tilde{G}_k^{(D)}(\vec{r}, \vec{r}_0)]. \tag{15}$$

If the forward data $\tilde{p}(\vec{r}_0, k)$ has been filtered using a filter $H(k)$, then using (4) the filtered reconstruction $p_{0_W}^{rec}(\vec{r})$ corresponding to a window function $W(k/k_c)$ can be written as

$$p_{0_W}^{rec}(\vec{r}) = \frac{1}{2\pi}\int_{-\infty}^{\infty} dk \int_{S_0} dS_0 \tilde{p}(\vec{r}_0, k) H(k)[\hat{n}_0^{S_0}.\vec{\nabla}_0 \tilde{G}_k^{(D)}(\vec{r}, \vec{r}_0)]. \quad (16)$$

The window function $W(k/k_c)$ used for filtering (6) can be expanded using a Taylor series as

$$W(k/k_c) = W(0) + \frac{k}{k_c}W'(0) + \left(\frac{k}{k_c}\right)^2 W''(0) + H.O.T., \quad (17)$$

where H.O.T. stands for "higher order terms". The window functions considered in this study attain the maxima at zero frequency ($W'(k = 0) = 0$) with W(k=0)=1. Substitution of this expansion in (16) gives

$$p_{0_W}^{rec}(\vec{r}) \approx \frac{1}{2\pi}\int_{-k_c}^{k_c} dk \int_{S_0} dS_0 \tilde{p}(\vec{r}_0, k)\left[1 + \left(\frac{k}{k_c}\right)^2 W''(0)\right][\hat{n}_0^{S_0}.\vec{\nabla}_0 \tilde{G}_k^{(D)}(\vec{r}, \vec{r}_0)], \quad (18)$$

where we have neglected the terms beyond the second order in the Taylor expansion of $W(k/k_c)$. Considering now the basic rectangular window, the band-limited reconstruction of the initial PA pressure can be written from (7) and (16) as

$$p_{0_{RW}}^{rec}(\vec{r}) = \frac{1}{2\pi}\int_{-k_c}^{k_c} dk \int_{S_0} dS_0 \tilde{p}(\vec{r}_0, k)[\hat{n}_0^{S_0}.\vec{\nabla}_0 \tilde{G}_k^{(D)}(\vec{r}, \vec{r}_0)]. \quad (19)$$

Thus from (18) and (19), we obtain

$$p_{0_W}^{rec}(\vec{r}) - p_{0_{RW}}^{rec}(\vec{r}) \approx \frac{1}{2\pi}\int_{-k_c}^{k_c} dk \int_{S_0} dS_0 \tilde{p}(\vec{r}_0, k)\left(\frac{k}{k_c}\right)^2 W''(0)[\hat{n}_0^{S_0}.\vec{\nabla}_0 \tilde{G}_k^{(D)}(\vec{r}, \vec{r}_0)]. \quad (20)$$

Substituting the value of $k^2\tilde{G}_k^{(D)}(\vec{r}, \vec{r}_0)$ from (13) into (20) gives

$$\begin{aligned} p_{0_W}^{rec}(\vec{r}) - p_{0_{RW}}^{rec}(\vec{r}) &\approx \frac{1}{2\pi}\int_{-k_c}^{k_c} dk \int_{S_0} dS_0 \tilde{p}(\vec{r}_0, k)\left(\frac{1}{k_c}\right)^2 W''(0) \\ &\qquad [\hat{n}_0^{S_0}.\vec{\nabla}_0(-\nabla^2 \tilde{G}_k^{(D)}(\vec{r}, \vec{r}_0) - \delta(\vec{r} - \vec{r}_0))] \\ &= \gamma_1(\vec{r}) + \gamma_2(\vec{r}), \end{aligned} \quad (21)$$

with,

$$\begin{aligned} \gamma_1(\vec{r}) &= \frac{1}{2\pi}\int_{-k_c}^{k_c} dk \int_{S_0} dS_0 \tilde{p}(\vec{r}_0, k)\left(\frac{1}{k_c}\right)^2 W''(0)[\hat{n}_0^{S_0}.\vec{\nabla}_0(-\nabla^2 \tilde{G}_k^{(D)}(\vec{r}, \vec{r}_0)] \\ &= -\left(\frac{W''(0)}{k_c^2}\right)\nabla^2 p_{0_{RW}}^{rec}(\vec{r}), \end{aligned} \quad (22)$$

where we have used the definition of $p_{0_{RW}}^{rec}(\vec{r})$ as in (19).

We now evaluate the second error term $\gamma_2(\vec{r})$,

$$\gamma_2(\vec{r}) = \frac{1}{2\pi}\int_{-k_c}^{k_c} dk \int_{S_0} dS_0 \tilde{p}(\vec{r}_0,k)\left(\frac{1}{k_c}\right)^2 W''(0)[\hat{n}_0^{S_0}.\vec{\nabla}_0(-\delta(\vec{r}-\vec{r}_0))]. \tag{23}$$

Let us consider an N-dimensional orthogonal curvilinear coordinate system with co-ordinates $(\xi_1, \xi_2, \dots \xi_N)$, scale factors $(h_1, h_2, \dots h_N)$ and corresponding unit vectors $(\hat{e}_1, \hat{e}_2, \dots, \hat{e}_N)$. Then the Dirac delta function can be expressed as [46]

$$\delta(\vec{r}-\vec{r}_0) = \frac{\delta(\xi_1-\xi_{10})}{h_1}\frac{\delta(\xi_2-\xi_{20})}{h_2}\dots\frac{\delta(\xi_N-\xi_{N0})}{h_N}. \tag{24}$$

Let $\xi_1 = \xi_{10}$ be the detection surface, $\hat{e}_1$ be the unit vector perpendicular the detection surface $(\hat{n}_0^{S_0})$ and the detector area element be given by $dS_0 = (h_2 h_3 \dots h_N)(d\xi_{20} d\xi_{30} \dots d\xi_{N0})$. We can thus write $\gamma_2(\vec{r})$ as

$$\begin{aligned}\gamma_2(\vec{r}) &= \frac{W''(0)}{2\pi k_c^2}\int_{-k_c}^{k_c} dk \int_{S_0} h_2 h_3 \dots h_N d\xi_{20} d\xi_{30} \dots d\xi_{N0} \tilde{p}(\vec{r}_0,k) \\ &\qquad \left[\hat{e}_1.\vec{\nabla}_0\Big(-\frac{\delta(\xi_1-\xi_{10})}{h_1}\dots\frac{\delta(\xi_N-\xi_{N0})}{h_N}\Big)\right] \\ &= \frac{W''(0)}{2\pi k_c^2}\int_{-k_c}^{k_c} dk \int_{S_0} d\xi_{20} d\xi_{30} \dots d\xi_{N0} \tilde{p}(\vec{r}_0,k)\Big[\delta(\xi_2-\xi_{20})\dots \\ &\qquad \dots\delta(\xi_N-\xi_{N0})\frac{\partial}{\partial\xi_1}\delta(\xi_1-\xi_{10})\Big].\end{aligned} \tag{25}$$

If the detection grid is not a part of domain of reconstruction, then $\xi_1 \neq \xi_{10} \implies \frac{\partial}{\partial\xi_1}\delta(\xi_1-\xi_{10}) = 0 \implies \gamma_2 = 0$. Hence

$$p_{0_W}^{rec}(\vec{r}) - p_{0_{RW}}^{rec}(\vec{r}) \approx \gamma_1(\vec{r}) = -\left(\frac{W''(0)}{k_c^2}\right)\nabla^2 p_{0_{RW}}^{rec}(\vec{r}). \tag{26}$$

Consider a discretized three dimensional image with $N_x \times N_y \times N_z$ voxels. The derived error (26) is a pointwise estimate but the Laplacian of the discretized reconstruction may lead to inaccurate results. Thus, the quality of reconstructions for a given filter can be quantified in terms of the averaged error$(\bar{\epsilon})$ (defined in (10)) as

$$\begin{aligned}\bar{\epsilon} &\triangleq \frac{1}{N_x N_y N_z}\sum_{i,j,k=0}^{N_x,N_y,N_z} |p_{0_W}^{rec}(i,j,k) - p_{0_{RW}}^{rec}(i,j,k)| \\ &= -\frac{1}{N_x N_y N_z}\left(\frac{W''(0)}{k_c^2}\right)\sum_{i,j,k=0}^{N_x,N_y,N_z} \bigtriangledown^2 p_{0_{RW}}^{rec}(x_i,y_j,z_k).\end{aligned} \tag{27}$$

One important aspect we notice from (27) is the linearity of $\bar{\epsilon}$ with respect to $W''(0)$ for a fixed cut-off frequency, which will be utilized in later sections. Moreover, this result holds only for commonly used smooth filters, otherwise the Taylor approximation of the filter used in the proof would be highly inaccurate.

4. Noisy data discrimination and appropriate filter cut-off frequencies

The forward PA signals first undergo band-limited filtering and then are fed into the UBP algorithm to obtain PA reconstructions. The band limited filters are characterized by a window function W and a cut off frequency k_c. Different window functions and cut off frequencies will lead to different reconstructions. We propose the averaged error $\bar{\epsilon}$ (27) as the measure of the performance of a filter in PA reconstruction.

The filters chosen in this work are

$$H_B(k) = \begin{cases} W_B(k/k_c) = B + (1-B)cos(\pi k/k_c) & : |k| < k_c \\ 0 & : otherwise \end{cases} , \qquad (28)$$

where H_B represents the class of Hamming filters with $0.5 \leq B \leq 1$.

Noiseless data characteristics: In the case of noiseless PA data, for a given cut-off frequency the rectangular window filtering leads to the best approximation to the PA source. The filters with higher $W''(0)$ will cause higher attenuation across frequencies than lower $W''(0)$ filters. Consequently, we have greater distortion in data and hence more reconstruction error while using high $W''(0)$ filtered forward data (figure 2d).

According to our proposed error estimate in (27), the averaged error $\bar{\epsilon}$ in PA reconstruction for a fixed cut-off frequency will be linearly dependent on the double derivative of the window function at Fourier origin $W''(0)$. Hence, we construct the best linear fit to average errors plotted with respect to a range of Hamming filters (indexed by B). When these reconstructions are carried out for several cut-off frequencies, the slopes of $\bar{\epsilon}$ vs $W''(0)$ are found to be increasing with decrement in cut-off frequencies because of the k_c^2 in the denominator.

Noisy data characteristics: In case of noisy PA data, we expect the proportionality of averaged error $\bar{\epsilon}$ for a fixed cut-off frequency with $W''(0)$ to be preserved. However, we do expect the noise effects to play a role in the slopes of the best fits. When a noisy data is filtered using a larger cut-off frequency, the high frequency amplitudes (noise) are included in the reconstruction. The band limited reconstruction with a high frequency content will lead to noisy artefacts in the reconstruction and hence to a high value of $\nabla^2 p_{0_{RW}}^{rec}(\vec{r})$. Consequently, for low SNR signals, the slopes for higher cut-off frequencies are expected to be higher than that for lower cut-off frequencies, which results in disordering in the $\bar{\epsilon}$ vs $W''(0)$ slopes as compared to the noiseless case. With improvement in SNR, the disorder of the slopes keeps decreasing until a certain high SNR, the ordering becomes the same as for noiseless data. Hence, we can consider the slope ordering as a qualitative measure of SNR of the PA signal.

Noisy data discrimination: Suppose that sets of photoacoustic forward data of the same object have been generated under different experimental and environmental conditions. Differing conditions will lead to different photoacoustic forward data. We can carry out the reconstructions using the bank of Hamming filters for these datasets at different cut-off frequencies and plot the averaged error $\bar{\epsilon}$ vs $W''(0)$. The slope ordering for each of these datasets goes back to that of the noiseless case for below a certain cut-off frequency. As per our observations of the previous paragraph, we see that the dataset with the best SNR is the one that maintains the slope-ordering (as for the noiseless data) for the maximum of the slope-order-maintaining cut-off frequencies.

Choice of appropriate cut-off frequency for a dataset: For a given data set, the $\bar{\epsilon}$ vs $W''(0)$ graph with different cut-off frequencies can assist in choosing an appropriate cut-off frequency. One chooses an appropriate cut-off frequency for a given PA data such that noise is significantly curtailed while reducing loss of critical data. Hence, the maximal cut-off frequency assuring the noiseless ordering of the slopes can be chosen as an appropriate cut-off frequency for a given noise level.

The present work has an ultimate objective of being able to design an appropriate reconstruction scheme for given data-acquisition settings with corresponding frequency domain effects ; we note that the effects such as source and detector bandwidth and acoustic-attenuation related frequency domain truncation can be modeled as low-pass/band-pass filtering operations. For instance, while in the present work we address the essential baseline case of ideal source and flat-passband detector settings, the presented approach can be conjectured to be generalized to data-sets representable in the form $h * p_{data}$ (for known experimental temporal-impulse-response $h(t)$ with $p_{data} \equiv p(\vec{r}_d, t)$ at detector position $\vec{r}_d$) via deconvolution and subsequent application of the above described algorithm.

5. Numerical studies

We validate our reconstruction characterization scheme with Hamming filter based reconstructions obtained for three numerical phantoms **P1, P2** and **P3** of the following specifications:

P1: A big cube (pressure source value 1 unit) with 9 small cuboids inside (pressure source value 2 units). (figure 2a, 3a)

P2: A big cylinder (pressure source value 1 unit) with 11 small cylinders (2 cylinders with pressure source value 0.5 unit, 6 cylinders with pressure source value 1.5 units and 3 cylinders with pressure source value 2 units) and 2 cuboids (pressure source value 2 units) inside.(figure 2b, 3b)

P3: A big cylinder (pressure source value 1 unit) with 23 small cylinders (10 cylinders with pressure source value 0.5 unit, 10 cylinders with pressure source value 1.5 units and 3 cylinders with pressure source value 2 units) and 8 cuboids (pressure source value 2 units) inside.(figure 2c, 3c).

The simulations were carried out in three different numerical settings:

Numerical Simulation 1 (Phantoms P1 and P2, spherical detection geometry, 8MHz sampling frequency): The measured PA signals are generated in a $401 \times 401 \times 401$ (voxels) domain with 0.1 mm resolution for 831 detector positions, spread uniformly on the surface of a sphere with radius 1.5cm at 8MHz sampling frequency using the function *"kspaceFirstOrder3D"* of the k-wave toolbox [47] for **P1** and **P2**. A criterion for proper simulation in the k-wave framework is that the smallest wavelength at which the wave propagation is simulated should be twice of the grid resolution. Therefore, for the given grid parameters the smallest wavelength at which the propagation can be supported is 0.2mm, which results in the maximum supported frequency for k-wave simulation $\approx$ 7.5 MHz. For the phantoms chosen in this simulation, the major contribution to the frequency spectrum of the received signal is found to be contained within 4MHz; the criterion used is a neglection of frequency components less than 1% of the maximum amplitude. Hence the sampling frequency chosen is 8MHz.

Numerical Simulation 2(Phantom P3, spherical detection geometry, 16MHz sampling frequency): The measured PA signals are generated in a $801 \times 801 \times 801$ (voxels) domain with 0.05 mm resolution for 1635 detector positions, spread uniformly on the surface of a sphere with radius 1.5cm at 16MHz sampling frequency using the function *"kspaceFirstOrder3D"* of the k-wave toolbox [47] for **P3**. Therefore, for the given grid parameters the smallest wavelength at which the propagation can be supported is 0.1 mm, which results in the maximum supported frequency for k-wave simulation $\approx$ 15 MHz. For the phantom chosen in this simulation, the major contribution to the frequency spectrum of the received signal is found to be contained within 8MHz. Hence the sampling frequency chosen is 16MHz.

Numerical Simulation 3 (Phantom P1 in two planar detection geometries, 8MHz sampling frequency): The measured PA signals are generated in a $601 \times 601 \times 601$ (voxels) domain with 0.1 mm resolution for **3A)** 2601 detectors and **3B)** 3969 detectors, spread uniformly on the surface of a square with side 10cm at 8MHz sampling frequency using the function *"kspaceFirstOrder3D"* of the k-wave toolbox [47] for **P1**.

5.1. *Validation of error estimates with noiseless data*

Universal back projection based PA inversions have been carried out for a series of filtered (using Hamming filter functions) forward data corresponding to the three numerical simulations. The Hamming window is defined as [48]

$$W_B(k) = B + (1 - B)cos(\pi k/k_c), \tag{29}$$

for $0.5 \leq B \leq 1$. Note that $B = 0.5$ and $B = 1$ for the Hanning and the rectangular windows respectively. Averaged errors $\bar{\epsilon}$ (27) are plotted with $W''(0)$ for each of the reconstructions as a quantification of the performances of different filters ($W''(0)$) (figure 4). The following propositions which were made in section 4 have been numerically validated.

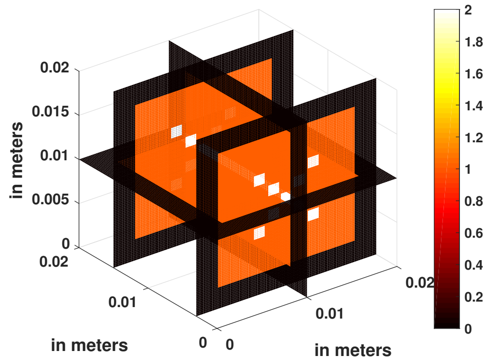

(a) 3D visualization of P1

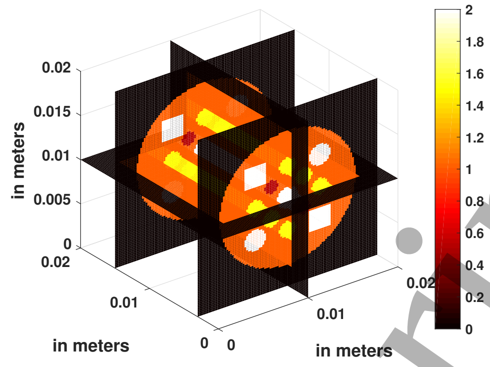

(b) 3D visualization of P2

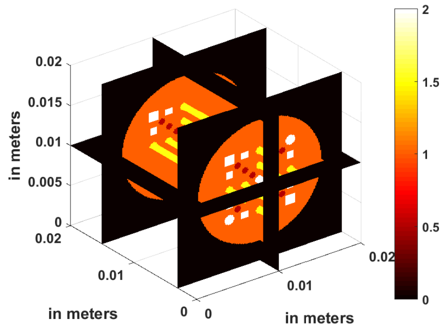

(c) 3D visualization of P3

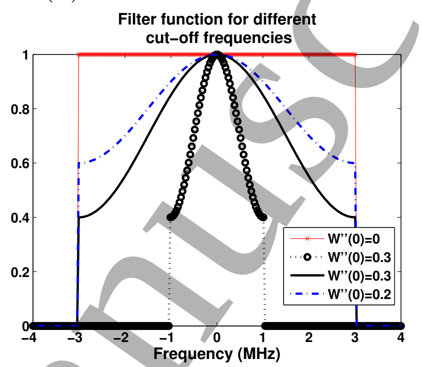

(d) Examples of filters used

Figure 2: Initial pressure sources and the filters used in this study

- For a fixed cut-off frequency window, the filters with higher $W''(0)$ lead to higher attenuation in the corresponding frequency amplitudes than lower $W''(0)$ filters. This leads to more loss of data and hence more error in reconstructions using high $W''(0)$ filtered forward data (figure 4).
- The slopes of $\bar{\epsilon}$ vs $W''(0)$ are found to be increasing with decrement of cut-off frequencies (figure 4). A similar ordering was found with UBP based PAT reconstructions with a planar detection geometry as well and reported in our previous work [28].

5.2. Noisy data discrimination and strategy for choice of the appropriate cut-off frequency for filtering

The filtering process of the forward data plays a major role in governing the accuracy of PA reconstructions from noisy data. Choosing a rectangular window over the complete frequency band for PA reconstruction leads to the best reconstruction, if the data is noiseless. However, doing so for low SNR data results in noise artifacts in the reconstruction. Moreover, employing a sharp window (a window function with high $W''(0)$) in a small frequency band leads to attenuation of useful signal and hence false reconstructions. A judicious choice of the filter function is thus critical for a good reconstruction. Figure 5a,5c are the reconstructions obtained from data with

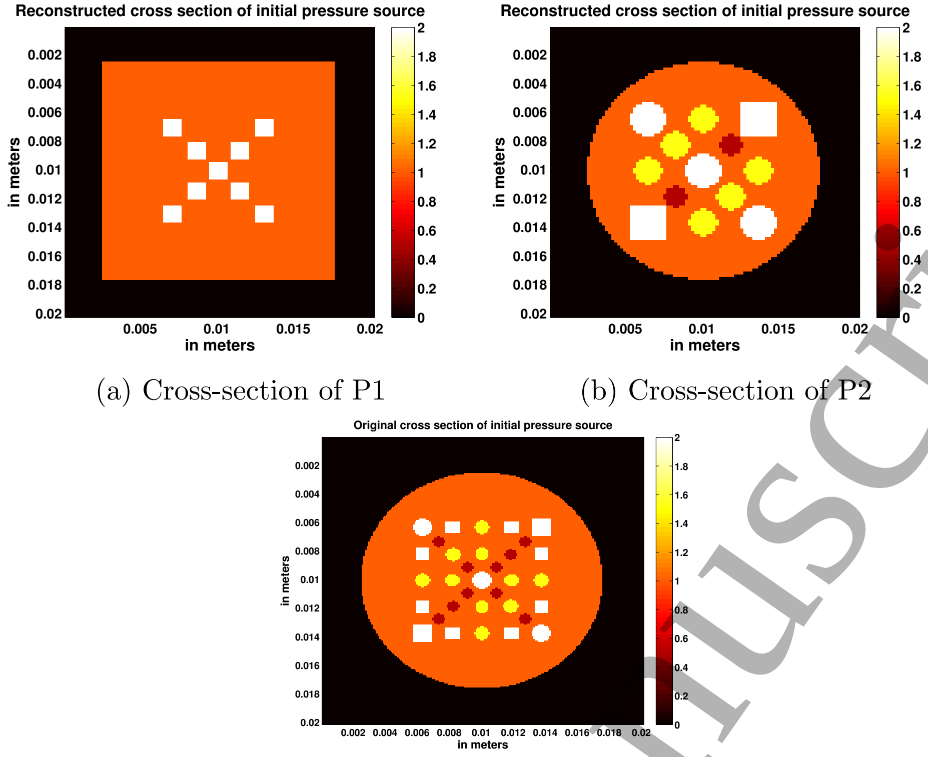

(a) Cross-section of P1 (b) Cross-section of P2

(c) Cross-section of P3

Figure 3: Cross-sections of initial pressure sources used in this study.

5dB SNR and all the frequencies participate in the reconstructions. Consequently, the noise artifacts are visible in the cross-sections. Figure 5b,5d depict the cross-sections reconstructed using the Hanning window (the steepest of all the Hamming windows) and 0.8 MHz cut-off frequency. The choice of a steep window with small cut-off frequency leads to loss of high frequency components as well as attenuation of several low frequency components of the PA signal. As a result, one can notice the missing characteristic features in the reconstructions thus obtained. The computed forward data for the phantoms were perturbed by white Gaussian noise to generate noisy data with desired SNRs. The noisy data are then filtered using a series of Hamming windows and universal back projection algorithm is used to carry out the PA reconstructions. Averaged errors $\bar{\epsilon}$ are plotted against $W''(0)$ (figure 6-10). Although, the proportionality of averaged error $\bar{\epsilon}$ with $W''(0)$ is preserved, the noisy effects manifest in a "*change in the ordering*" of the slopes of the best fits, with respect to that observed for noiseless data reconstructions, where the slopes of the best-fit lines are found to increase with decrement in the cut-off frequencies. As proposed in section 4, we observe that for low SNR signals, the slopes for higher cut-off frequencies are higher than that for lower cut-off frequencies (figure 6-10). As the quality of signals improve (higher SNRs), the disorder of the slopes keeps decreasing upto a certain high SNR, where the ordering becomes same as for noiseless data (figure 6-10).

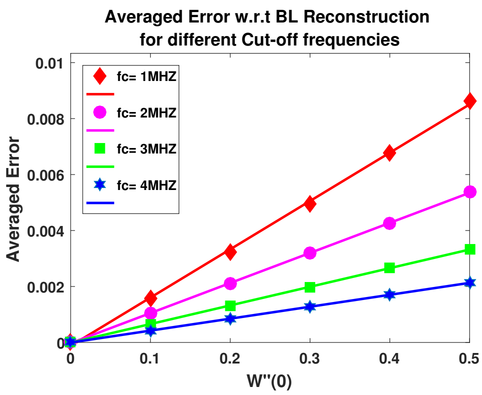

(a) Simulation 1: for P1 in spherical geometry

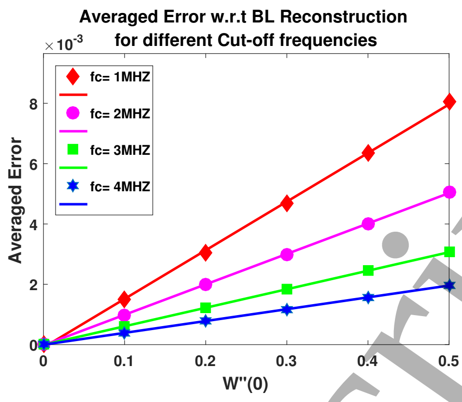

(b) Simulation 1: for P2 in spherical geometry

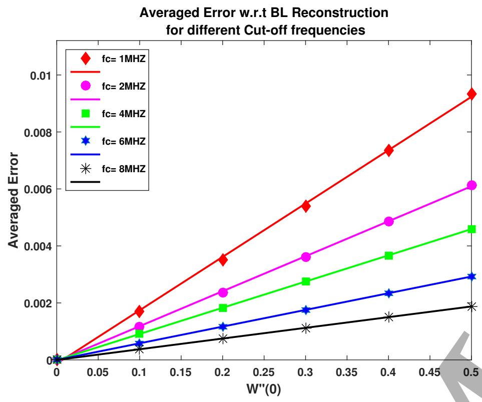

(c) Simulation 2: for P3 in spherical geometry

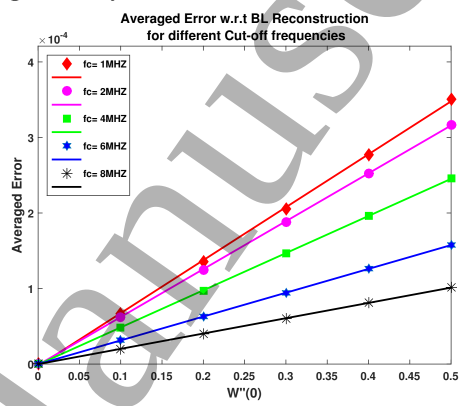

(d) Simulation 3A: for P1 in planar geometry

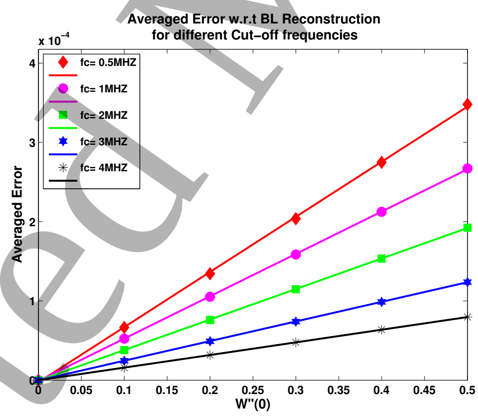

(e) Simulation 3B: for P1 in planar geometry

Figure 4: Plot of averaged error with $W''(0)$ for noiseless PA data.

We further utilize the method proposed in section 4 to choose an appropriate cut-off frequency k_c^a for a rectangular window reconstruction. For the phantoms considered in this study, the $\bar{\epsilon}$ w.r.t. $W''(0)$ plots obtained from reconstructions of the phantoms **P1 and P2** are given in figure 6-10. We intend to choose the maximum cut-off frequency

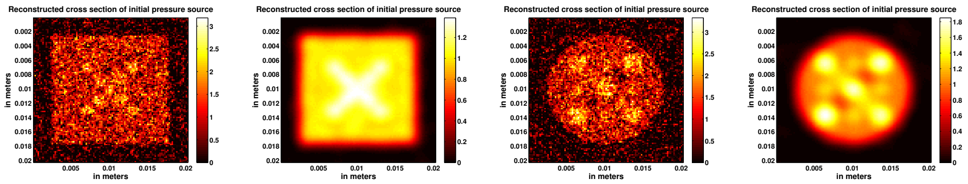

(a) (b) (c) (d)

Figure 5: Reconstruction of P1 from PA data (5dB SNR)(a)Rectangular window over 4.0 MHz cut-off (b)Hanning window over 0.8 MHz cut-off frequency; Reconstruction of P2 from PA data (5dB SNR)(a)RW window over 4.0 MHz cut-off (b)Hanning window over 0.8 MHz cut-off frequency

Table 1: **Simulation 1:**Appropriate cut-off frequency for the phantoms at different SNRs.

Appropriate cut-off frequency table for simulation 1					
Phantom	**SNR**(dB)	k_c^a(MHz)	**Phantom**	**SNR**(dB)	k_c^a(MHz)
P1	5	1.0	**P2**	5	1.0
	10	1.4		10	1.4
	15	1.8		15	2.1
	20	3.0		20	3.0

where the signature of noise, that is the perturbation in slope ordering is minimal. In other words considering that slope is inversely proportional to k_c^2, we need to find the cut-off frequency that corresponds to the minimum of the slope vs cut-off frequency graph (figure 11-15). The variation of slopes for a range of cut-off frequencies from 0.5 MHz to 4.0 MHz was first coarsely explored. The region around the minimum of the "cut-off frequency - slope curve" (indicated by the rectangles in figure 11-15), was then probed at a finer cut-off frequency discretization of 0.1 MHz. In our computational experience, we found that minor changes in the choice of k_c around the minimum, do not significantly affect the reconstructed cross-sections. Therefore the minimum of the "cut-off frequency - slope curve" (k_c^a, the appropriate cut-off frequency) was chosen by inspection, as a high precision is not desired in the choice.

The appropriate cut-off frequencies (k_c^a) obtained for the three sets of numerical simulations are tabulated in table 1,2,3.

The choices of the appropriate cut-off frequencies for 5dB, 10dB and 15dB SNRs are justified by the reconstructions provided in figure 16-20. The first column (figure 16a, 16d, 16g; figure 17a, 17d, 17g; figure 18a, 18d, 18g; figure 19a, 19d and figure 20a, 20d) and the second column (figure 16b, 16e, 16h; figure 17b, 17e, 17h; figure 18b, 18e, 18h; figure 19b, 19e and figure 20b, 20e) show the reconstructed cross-sections using lower and higher cut-off frequencies than the corresponding k_c^a respectively, while the reconstructions obtained using corresponding appropriate cut-off frequencies are provided in the third column (figure 16c, 16f, 16i; figure 17c, 17f, 17i;

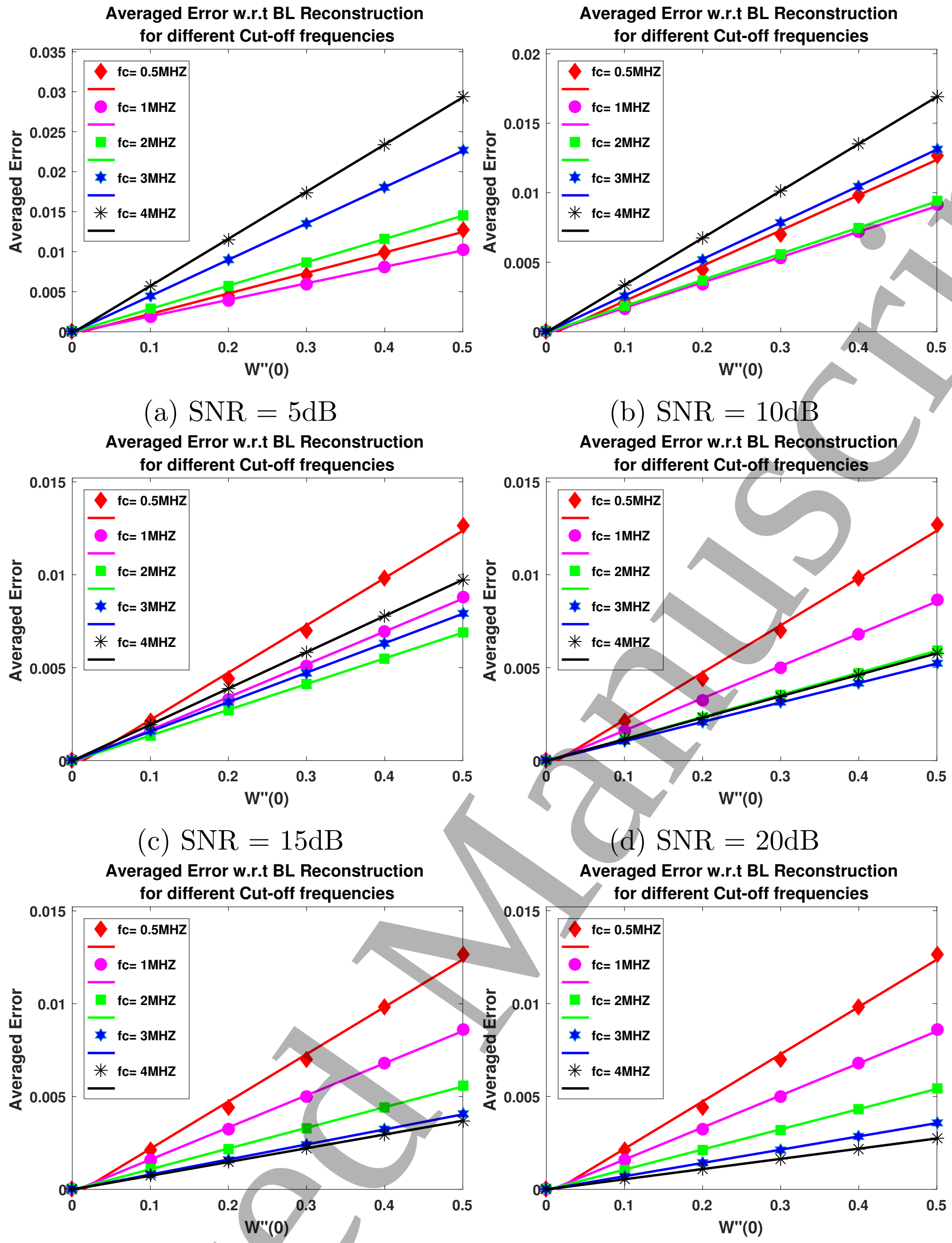

(a) SNR = 5dB (b) SNR = 10dB

(c) SNR = 15dB (d) SNR = 20dB

(e) SNR = 25dB (f) SNR = 30dB

Figure 6: **Simulation 1:** Averaged error for phantom P1 in spherical detection geometry (noisy forward data)

figure 18c, 18f, 18i;figure 19c, 19f and figure 20c, 20f).

The three-dimensional reconstructions obtained for the three simulations using appropriate cut-off frequencies (k_c^a) for different SNRs are depicted in figure 21.

Evaluation of accuracy of the reconstructions has been done on the basis of the

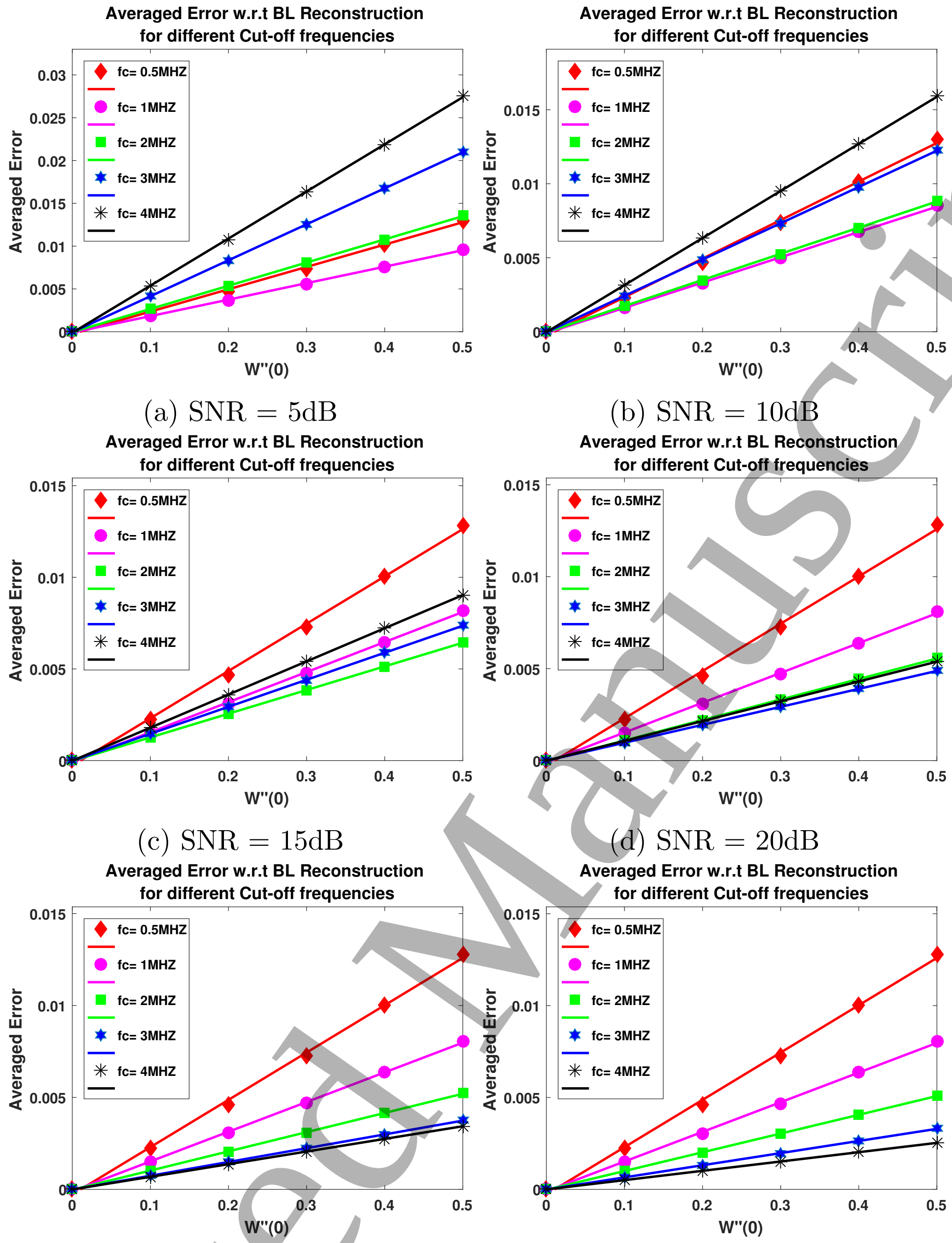

(a) SNR = 5dB (b) SNR = 10dB

(c) SNR = 15dB (d) SNR = 20dB

(e) SNR = 25dB (f) SNR = 30dB

Figure 7: **Simulation 1:** Averaged error for phantom P2 in spherical detection geometry (noisy forward data)

correlation coefficient(ρ) and the *deviation factor* (δ) defined as [49, 50]:

$$\rho = \frac{\sum_{i=1}^{N}(p_i^r - \bar{p}^r)(p_i^t - \bar{p}^t)}{(N-1)\triangle p^r \triangle p^t} \tag{30}$$

$$\delta = \frac{\sqrt{\sum_{i=1}^{N}(p_i^r - p_i^t)^2/N}}{\triangle p^t} \tag{31}$$

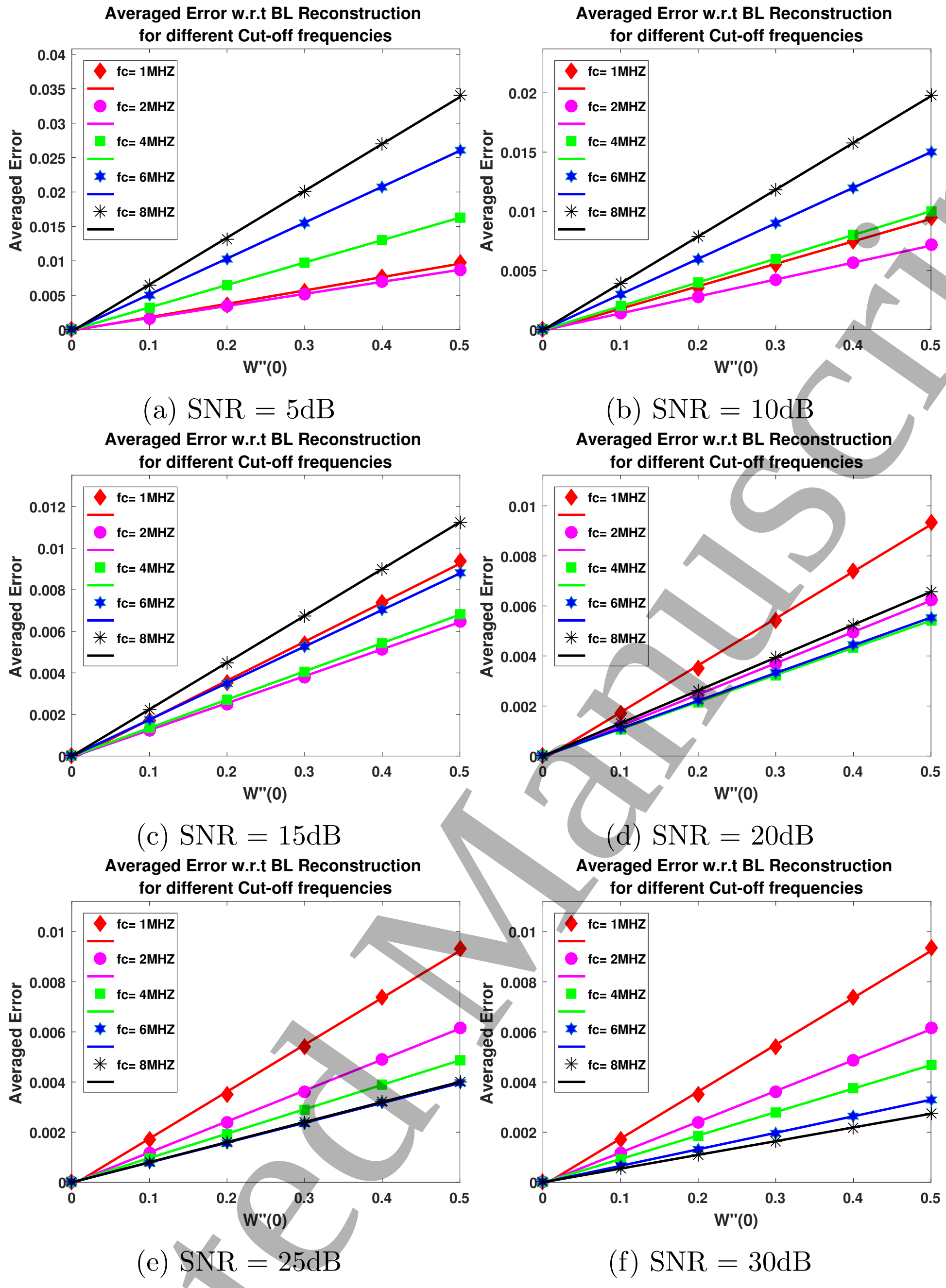

(a) SNR = 5dB (b) SNR = 10dB (c) SNR = 15dB (d) SNR = 20dB (e) SNR = 25dB (f) SNR = 30dB

Figure 8: **Simulation 2:** Averaged error for phantom P3 in spherical detection geometry (noisy forward data)

where N is the total number of voxels, $\triangle p^t$ and $\triangle p^r$ are the standard deviations and $\bar{p}^t$ and $\bar{p}^r$ are the mean values of the reference and reconstructed values of the parameter respectively. In this work, we provide two sets of correlation coefficients (ρ^o and ρ^r) and deviation factors (δ^o,δ^r) in the the regions of interest, where subscripts o and r denote that the true phantom and the noiseless full bandwidth rectangular window reconstruction were chosen as reference. We observed that the quality of the reconstruction improves significantly when the proposed appropriate cut-off frequency

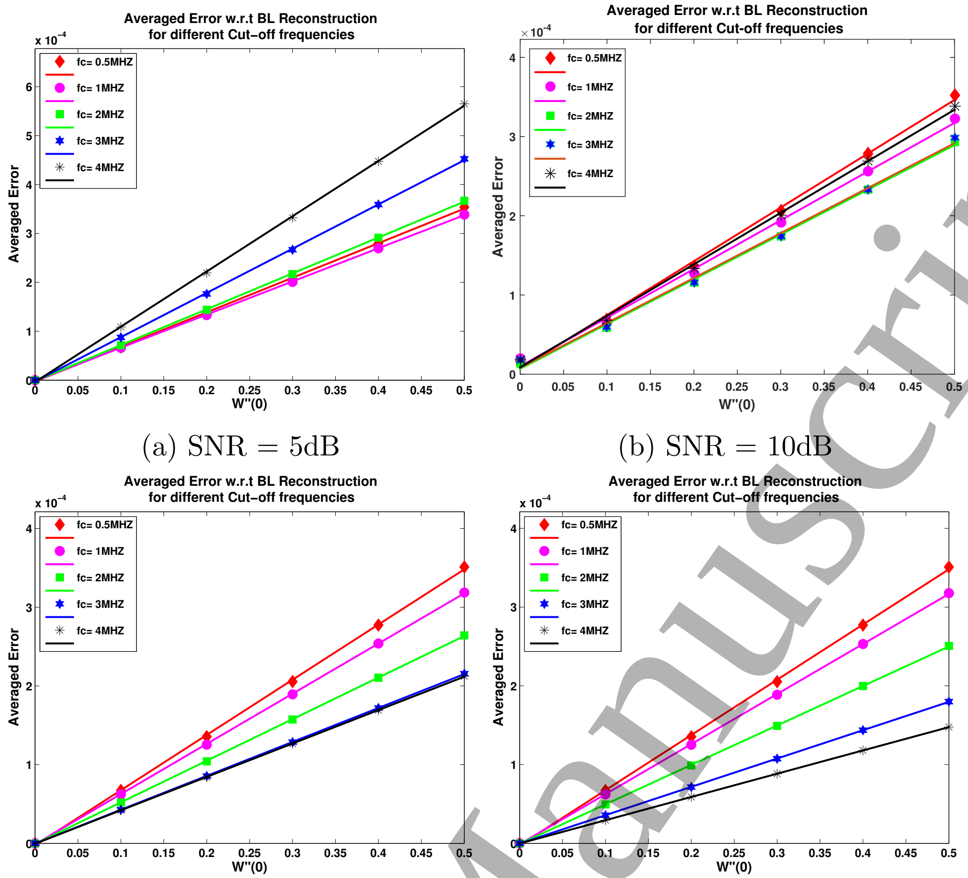

(a) SNR = 5dB (b) SNR = 10dB

(c) SNR = 15dB (d) SNR = 20dB

Figure 9: **Simulation 3A:** Averaged error for phantom P1 in planar detection geometry with 2601 detectors(noisy forward data)

Table 2: **Simulation 2:**Appropriate cut-off frequency for the phantoms at different SNRs.

Appropriate cut-off frequency table for simulation 2		
Phantom	**SNR**(dB)	k_c^a(MHz)
P3	5	1.8
	10	2.2
	15	2.6
	20	4.8

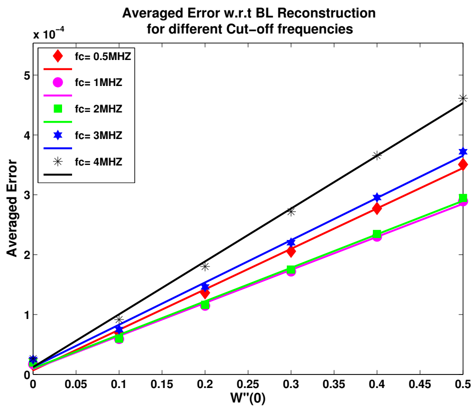

(a) SNR = 5dB

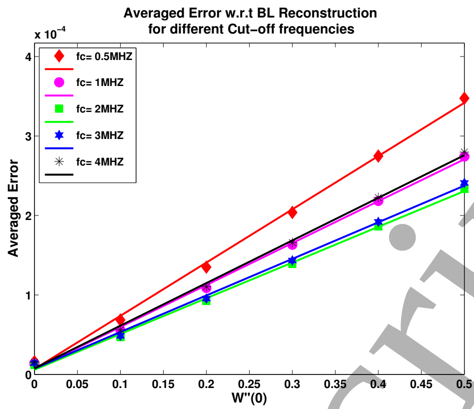

(b) SNR = 10dB

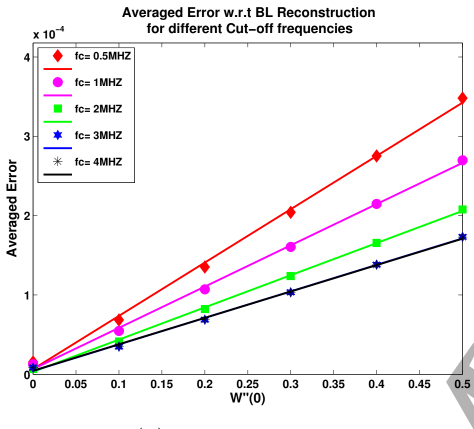

(c) SNR = 15dB

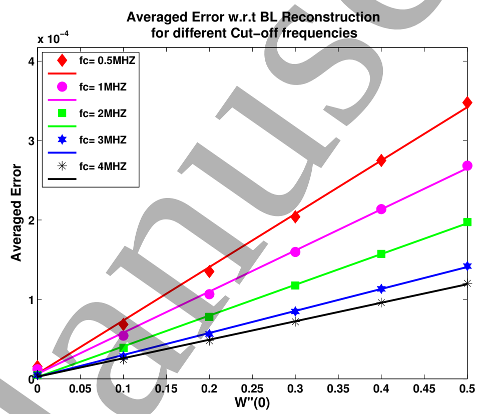

(d) SNR = 20dB

Figure 10: **Simulation 3B:** Averaged error for phantom P1 in planar detection geometry with 3969 detectors (noisy forward data)

Table 3: **Simulation 3:**Appropriate cut-off frequency for the phantoms at different SNRs.

Appropriate cut-off frequency table for simulation 3					
3A) 2601 detectors			**3B)** 3969 detectors		
Phantom	**SNR**(dB)	k_c^a(MHz)	**Phantom**	**SNR**(dB)	k_c^a(MHz)
P1	5	1.2	**P1**	5	1.5
	10	1.6		10	1.8

is chosen for the reconstructions (table 4, 5, 6).

We observe that our algorithm for the choice of appropriate cut-off frequency works well for all the numerical studies performed. However, we do notice that in the planar detection geometry (simulation 3) the reconstructions obtained are less sensitive to the choice of cut-off frequency as compared to the spherical detection geometry.

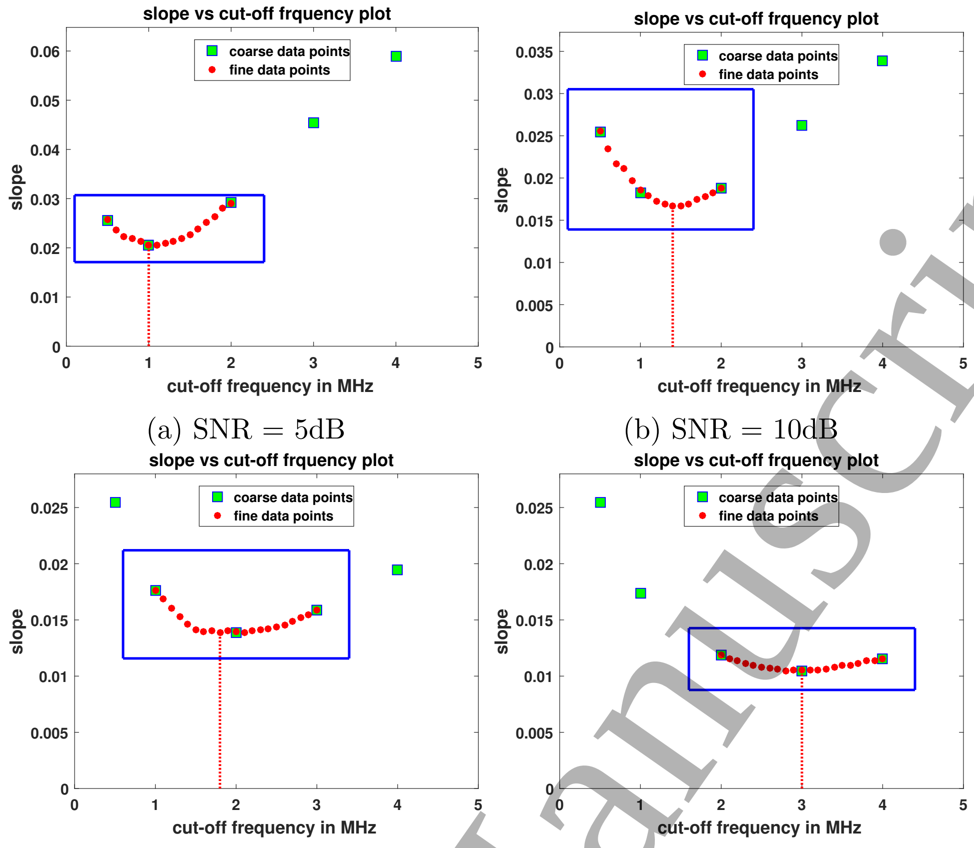

(a) SNR = 5dB (b) SNR = 10dB

(c) SNR = 15dB (d) SNR = 20dB

Figure 11: **Simulation 1:** Variation of slopes with cut-off frequency for phantom P1. The rectangle indicates the region, which has been finely explored to obtain the k_c^a

Table 4: Correlation coefficient ρ and deviation factor δ for reconstructions of simulation 1; ρ and δ obtained using k_c^a are given in boldface.

Simulation 1: Correlation coefficients and deviation factors													
Phantom	**SNR[dB]**	k_c **[MHz]**	ρ	δ	ρ	δ	**Phantom**	**SNR[dB]**	k_c**[MHz]**	ρ^o	δ^o	ρ^r	δ^r
P1	5	0.5	0.38	1.13	0.61	0.86	**P2**	5	0.5	0.72	0.76	0.86	0.54
		2.0	0.52	1.23	0.71	1.00			2.0	0.72	0.82	0.82	0.71
		1.0	**0.66**	**0.87**	**0.90**	**0.50**			1.0	**0.80**	**0.64**	**0.93**	**0.39**
	10	0.5	0.39	1.12	0.62	0.85		10	0.5	0.73	0.75	0.86	0.53
		2.0	0.64	0.93	0.87	0.58			2.0	0.80	0.64	0.93	0.40
		1.4	**0.69**	**0.83**	**0.93**	**0.42**			1.4	**0.83**	**0.59**	**0.96**	**0.30**
	15	1.0	0.70	0.80	0.95	0.33		15	1.0	0.83	0.59	0.96	0.29
		3.0	0.65	0.92	0.88	0.54			3.0	0.81	0.63	0.94	0.38
		1.8	**0.71**	**0.79**	**0.96**	**0.31**			2.1	**0.84**	**0.58**	**0.97**	**0.25**

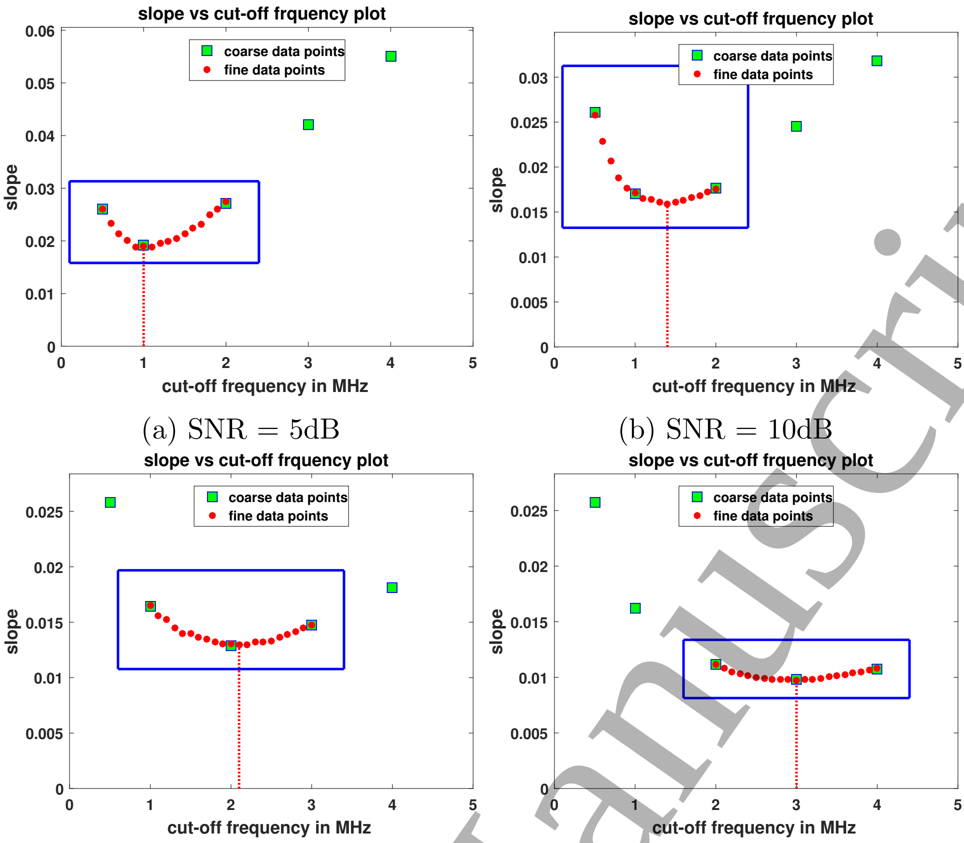

(a) SNR = 5dB (b) SNR = 10dB

(c) SNR = 15dB (d) SNR = 20dB

Figure 12: **Simulation 1:** Variation of slopes with cut-off frequency for phantom P2. The rectangle indicates the region, which has been finely explored to obtain the k_c^a

Table 5: Correlation coefficient ρ and deviation factor δ for reconstructions of simulation 2; ρ and δ obtained using k_c^a are given in boldface.

Simulation 2: Correlation coefficients and deviation factors						
Phantom	**SNR[dB]**	k_c **[MHz]**	ρ^o	δ^o	ρ^r	δ^r
P3	5	1	0.71	0.75	0.85	0.60
		4.0	0.57	1.20	0.68	1.09
		1.8	**0.77**	**0.69**	**0.89**	**0.50**
	10	1	0.72	0.74	0.85	0.59
		4.0	0.71	0.83	0.65	0.62
		2.2	**0.80**	**0.64**	**0.93**	**0.41**
	15	1.0	0.72	0.73	0.86	0.58
		4.0	0.78	0.67	0.94	0.36
		2.6	**0.82**	**0.61**	**0.97**	**0.25**

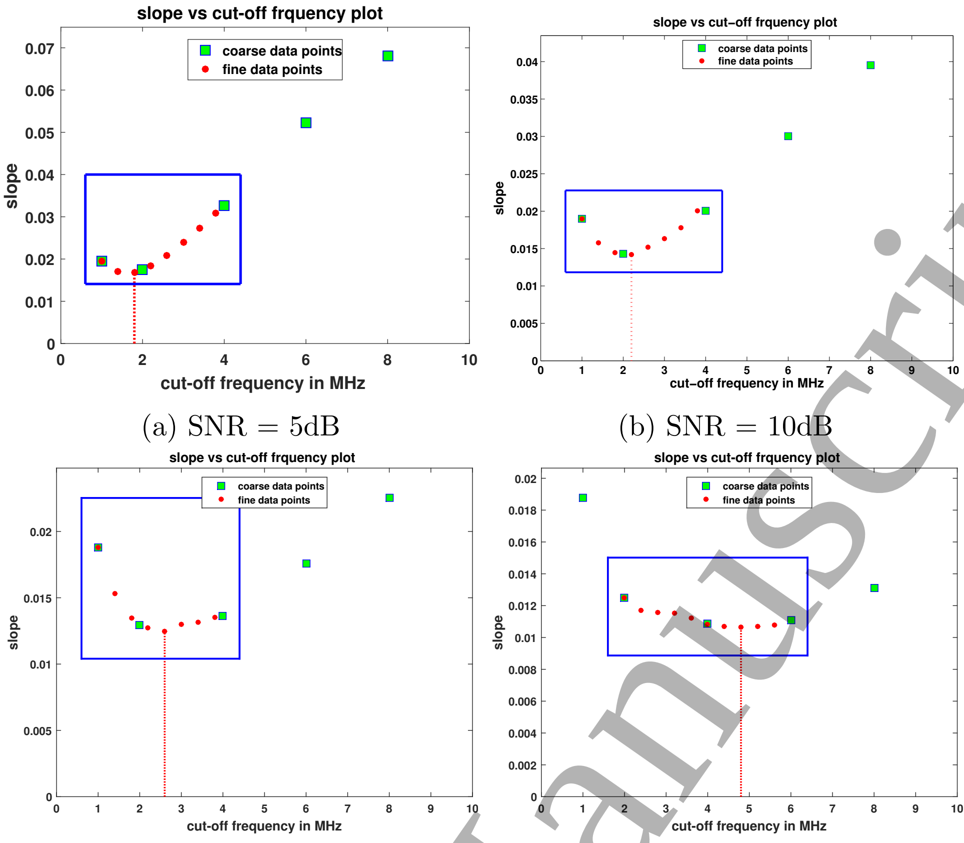

(a) SNR = 5dB (b) SNR = 10dB

(c) SNR = 15dB (d) SNR = 20dB

Figure 13: **Simulation 2:** Variation of slopes with cut-off frequency for phantom P3. The rectangle indicates the region, which has been finely explored to obtain the k_c^a

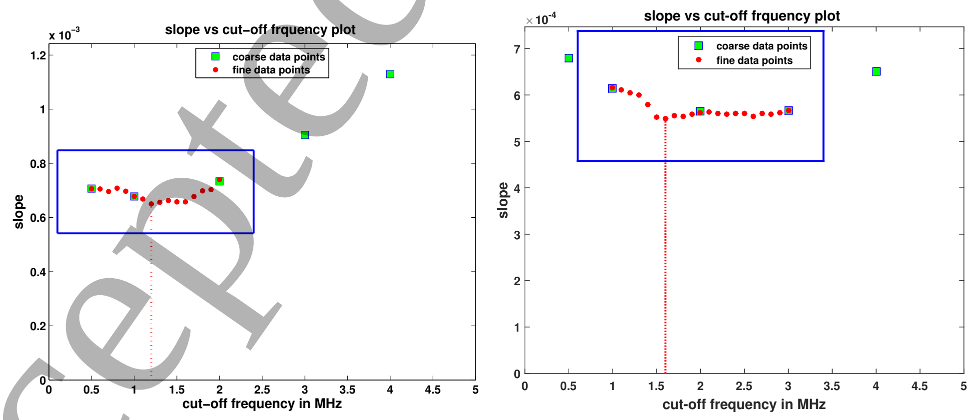

(a) SNR = 5dB (b) SNR = 10dB

Figure 14: **Simulation 3A:** Variation of slopes with cut-off frequency for phantom P1 (planar detection geometry). The rectangle indicates the region, which has been finely explored to obtain the k_c^a

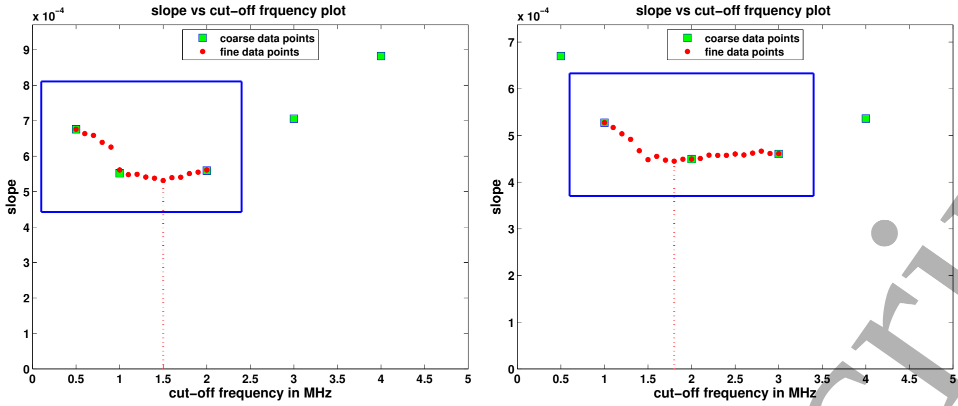

(a) SNR = 5dB (b) SNR = 10dB

Figure 15: **Simulation 3B:** Variation of slopes with cut-off frequency for phantom P1 (planar detection geometry). The rectangle indicates the region, which has been finely explored to obtain the k_c^a

Table 6: Correlation coefficient ρ and deviation factor δ for reconstructions of simulation 3; ρ and δ obtained using k_c^a are given in boldface.

Simulation 3: Correlation coefficients and deviation factors													
3A)2601 detectors							**3B)** 3969 detectors						
Phantom	**SNR[dB]**	k_c **[MHz]**	ρ^o	δ^o	ρ^r	δ^r	**Phantom**	**SNR[dB]**	k_c**[MHz]**	ρ^o	δ^o	ρ^r	δ^r
P1	5	0.5	0.36	1.43	0.62	0.85	**P1**	5	0.5	0.36	1.43	0.65	0.80
		2.0	0.58	1.33	0.93	0.37			2	0.61	1.26	0.95	0.30
		1.2	**0.61**	**1.27**	**0.95**	**0.35**			1.5	**0.62**	**1.24**	**0.96**	**0.28**
	10	1.0	0.61	1.25	0.94	0.38		10	1.0	0.61	1.24	0.96	0.29
		3.0	0.59	1.33	0.95	0.33			3.0	0.61	1.26	0.96	0.27
		1.6	**0.61**	**1.26**	**0.96**	**0.27**			1.8	**0.63**	**1.22**	**0.98**	**0.20**

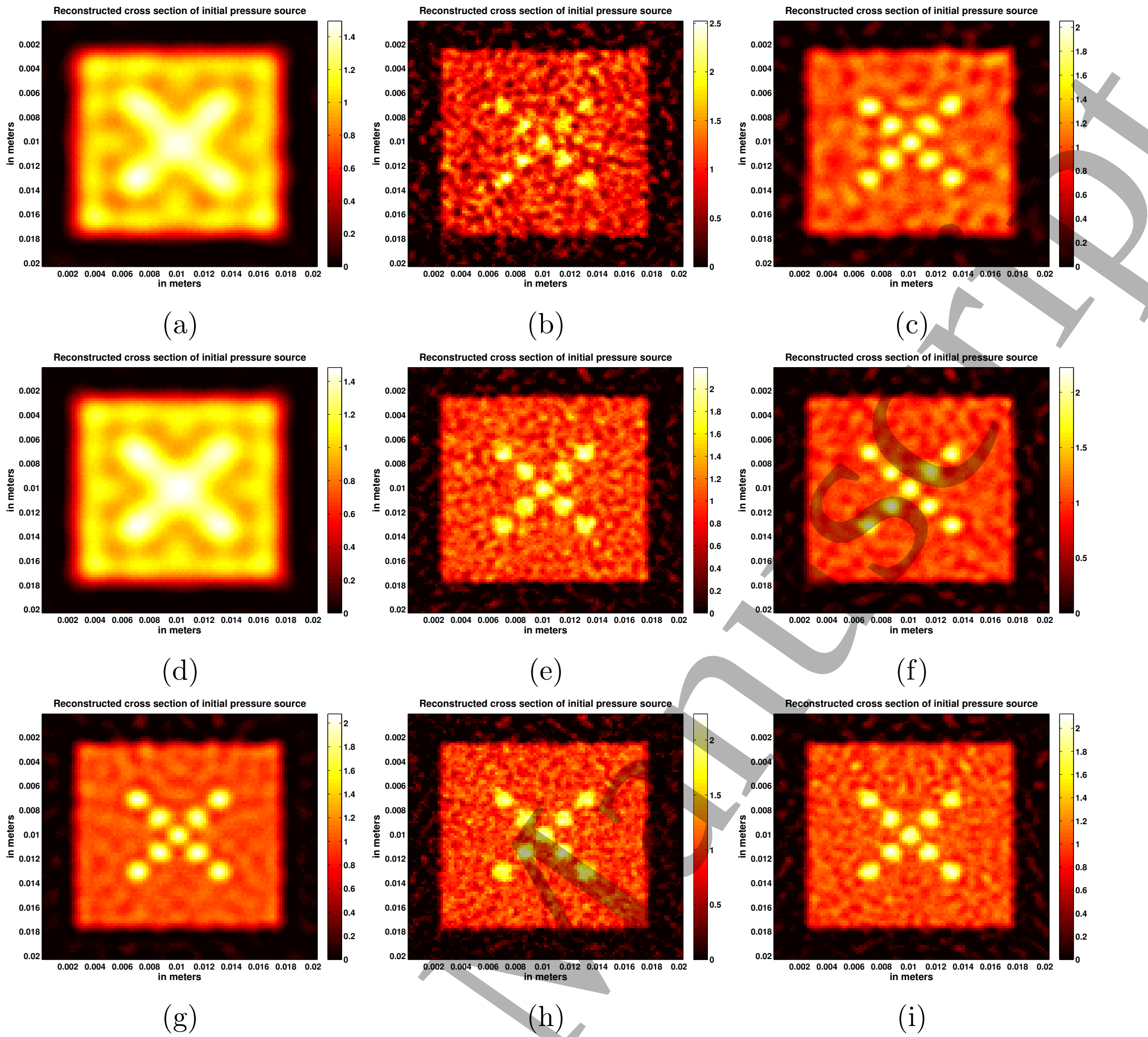

Figure 16: Numerical simulation 1: Cross-section of rectangular window reconstruction of **P1** using PA data with (a) 5dB SNR and $k_c = 0.5$ MHz ($\rho^o = 0.38, \delta^o = 1.13$)(b)5dB SNR and $k_c = 2.0$ MHz ($\rho^o = 0.52, \delta^o = 1.23$) (c) 5dB SNR and $k_c = k_c^a = 1.0$ MHz ($\rho^o = 0.66, \delta^o = 0.87$) (d) 10dB SNR and $k_c = 0.5$ MHz ($\rho^o = 0.39, \delta^o = 1.12$) (e) 10dB SNR and $k_c = 2.0$ MHz ($\rho^o = 0.64, \delta^o = 0.93$) (f)10dB SNR and $k_c = k_c^a = 1.4$ MHz ($\rho^o = 0.69, \delta^o = 0.83$) (g)15dB SNR and $k_c = 1.0$ MHz ($\rho^o = 0.70, \delta^o = 0.80$) (h)15dB SNR and $k_c = 3.0$ MHz ($\rho^o = 0.65, \delta^o = 0.92$)(i) 15dB SNR and $k_c = k_c^a = 1.8$ MHz ($\rho^o = 0.71, \delta^o = 0.79$)

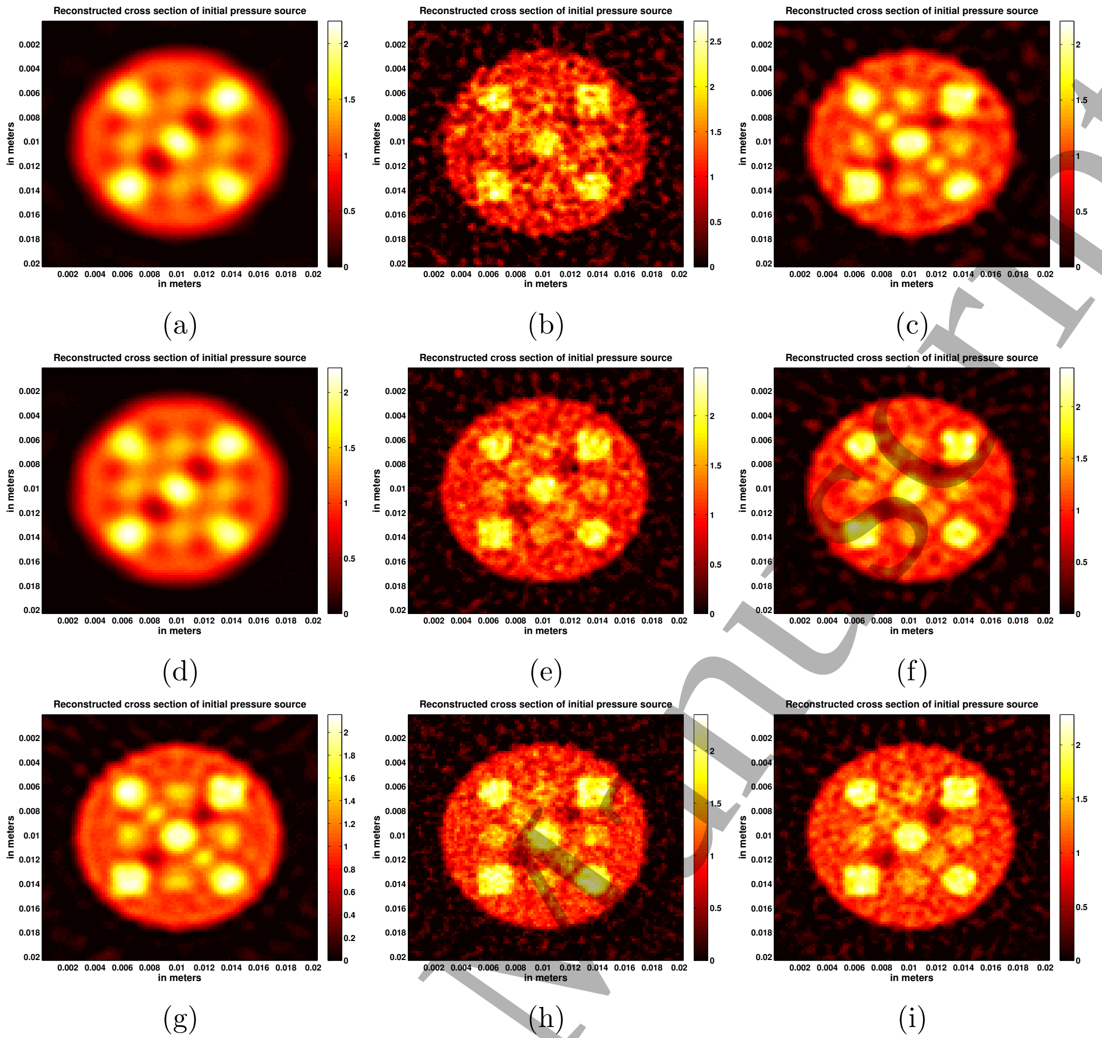

Figure 17: Numerical simulation 1: Cross-section of rectangular window reconstruction of **P2** using PA data with (a) 5dB SNR and $k_c = 0.5$ MHz ($\rho^o = 0.72, \delta^o = 0.76$)(b)5dB SNR and $k_c = 2.0$ MHz ($\rho^o = 0.72, \delta^o = 0.82$) (c) 5dB SNR and $k_c = k_c^a = 1.0$ MHz ($\rho^o = 0.80, \delta^o = 0.64$) (d) 10dB SNR and $k_c = 0.5$ MHz ($\rho^o = 0.73, \delta^o = 0.75$) (e) 10dB SNR and $k_c = 2.0$ MHz ($\rho^o = 0.80, \delta^o = 0.64$) (f)10dB SNR and $k_c = k_c^a = 1.4$ MHz ($\rho^o = 0.83, \delta^o = 0.59$) (g)15dB SNR and $k_c = 1.0$ MHz ($\rho^o = 0.83, \delta^o = 0.59$) (h)15dB SNR and $k_c = 3.0$ MHz ($\rho^o = 0.81, \delta^o = 0.63$)(i) 15dB SNR and $k_c = k_c^a = 2.1$ MHz ($\rho^o = 0.84, \delta^o = 0.58$)

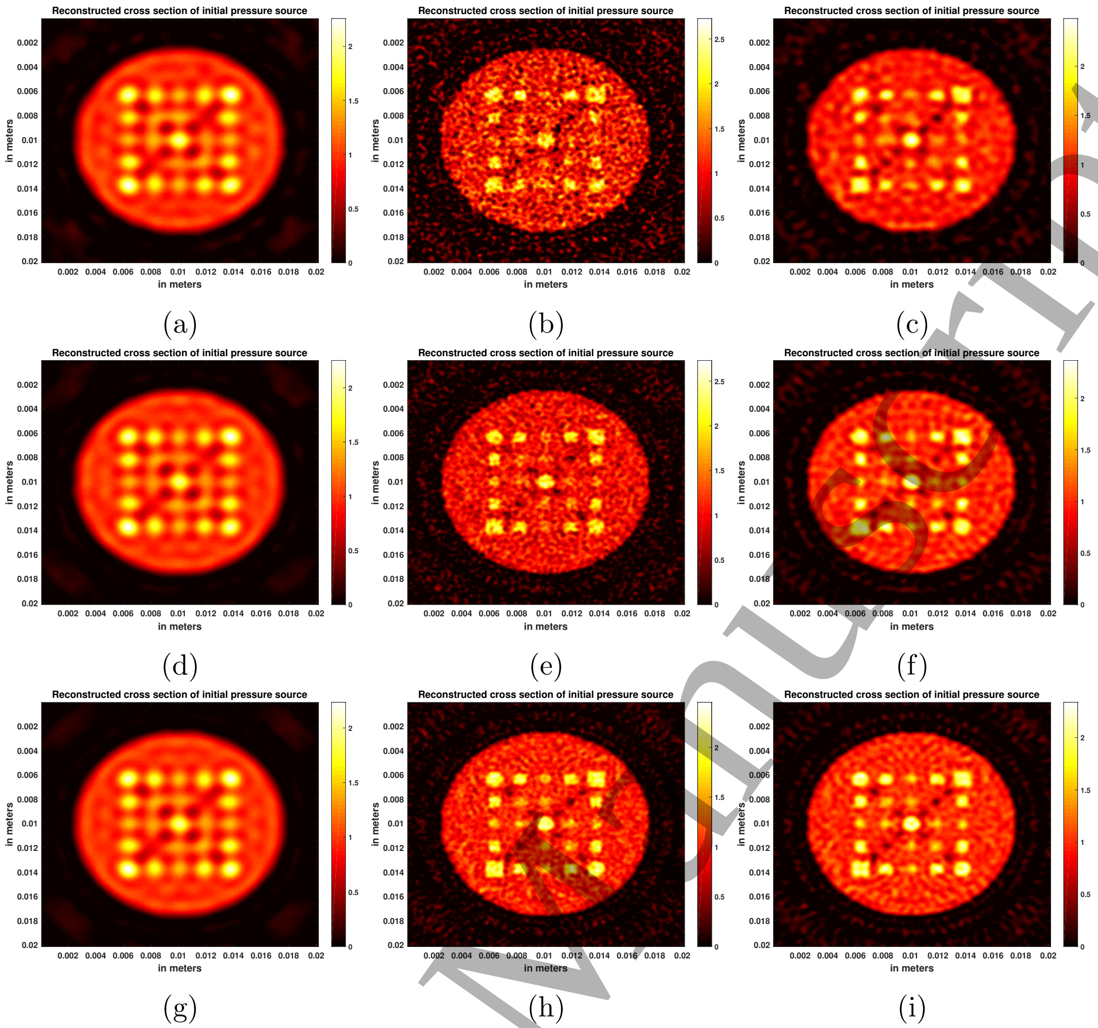

Figure 18: Numerical simulation 2: Cross-section of rectangular window reconstruction of **P3** using PA data with (a) 5dB SNR and $k_c = 1.0$ MHz ($\rho^o = 0.71, \delta^o = 0.75$)(b)5dB SNR and $k_c = 4.0$ MHz ($\rho^o = 0.57, \delta^o = 1.20$) (c) 5dB SNR and $k_c = k_c^a = 1.8$ MHz ($\rho^o = 0.77, \delta^o = 0.69$) (d) 10dB SNR and $k_c = 1.0$ MHz ($\rho^o = 0.72, \delta^o = 0.74$) (e) 10dB SNR and $k_c = 4.0$ MHz ($\rho^o = 0.71, \delta^o = 0.83$) (f)10dB SNR and $k_c = k_c^a = 2.2$ MHz ($\rho^o = 0.80, \delta^o = 0.64$) (g)15dB SNR and $k_c = 1.0$ MHz ($\rho^o = 0.72, \delta^o = 0.73$) (h)15dB SNR and $k_c = 4.0$ MHz ($\rho^o = 0.78, \delta^o = 0.67$)(i) 15dB SNR and $k_c = k_c^a = 2.6$ MHz ($\rho^o = 0.82, \delta^o = 0.61$)

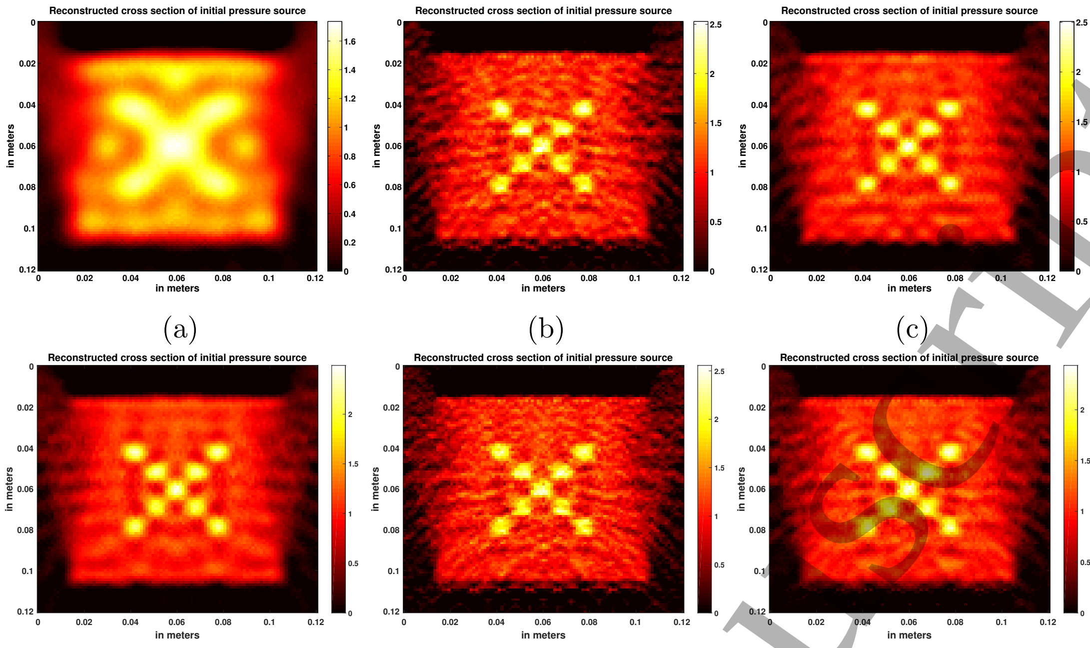

(a) (b) (c)

(d) (e) (f)

Figure 19: Numerical simulation 3A: Cross-section of rectangular window reconstruction of **P1** using PA data with (a) 5dB SNR and $k_c = 0.5$ MHz $(\rho^o = 0.36, \delta^o = 1.43)$(b)5dB SNR and $k_c = 2.0$ MHz $(\rho^o = 0.58, \delta^o = 1.33)$ (c) 5dB SNR and $k_c = k_c^a = 1.2$ MHz $(\rho^o = 0.61, \delta^o = 1.27)$ (d) 10dB SNR and $k_c = 1.0$ MHz $(\rho^o = 0.61, \delta^o = 1.25)$ (e) 10dB SNR and $k_c = 3.0$ MHz $(\rho^o = 0.59, \delta^o = 1.33)$ (f)10dB SNR and $k_c = k_c^a = 1.6$ MHz $(\rho^o = 0.61, \delta^o = 1.26)$

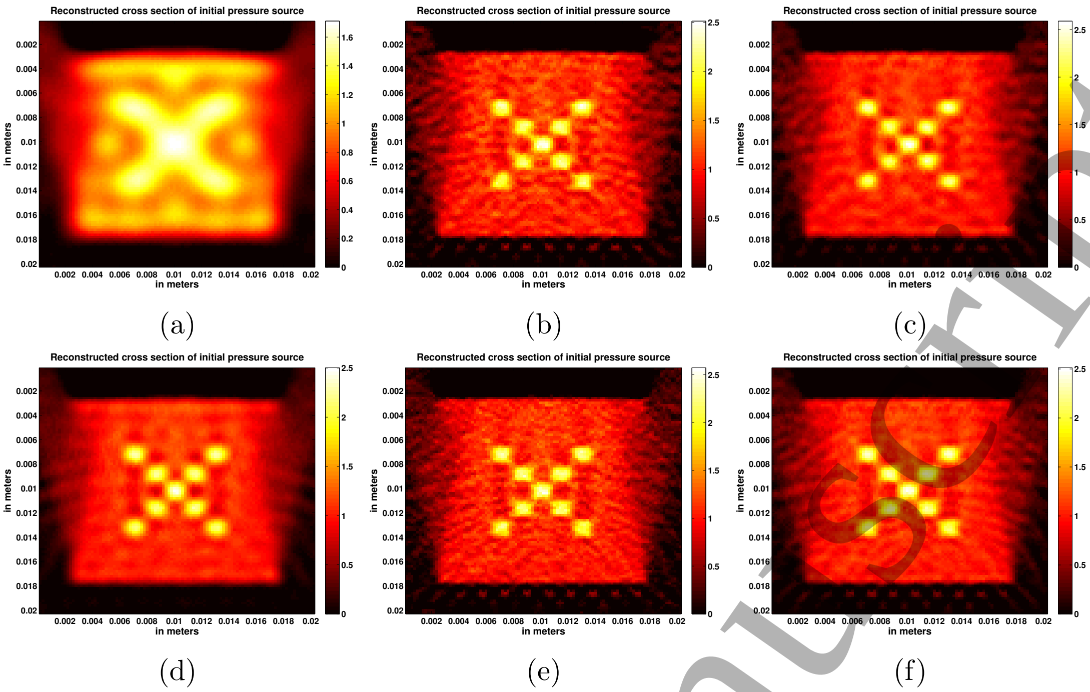

Figure 20: Numerical simulation 3B: Cross-section of rectangular window reconstruction of **P1** using PA data with (a) 5dB SNR and $k_c = 0.5$ MHz $(\rho^o = 0.36, \delta^o = 1.43)$(b)5dB SNR and $k_c = 2.0$ MHz $(\rho^o = 0.61, \delta^o = 1.26)$ (c) 5dB SNR and $k_c = k_c^a = 1.5$ MHz $(\rho^o = 0.62, \delta^o = 1.24)$ (d) 10dB SNR and $k_c = 1.0$ MHz $(\rho^o = 0.61, \delta^o = 1.24)$ (e) 10dB SNR and $k_c = 3.0$ MHz $(\rho^o = 0.61, \delta^o = 1.26)$ (f)10dB SNR and $k_c = k_c^a = 1.8$ MHz $(\rho^o = 0.63, \delta^o = 1.22)$

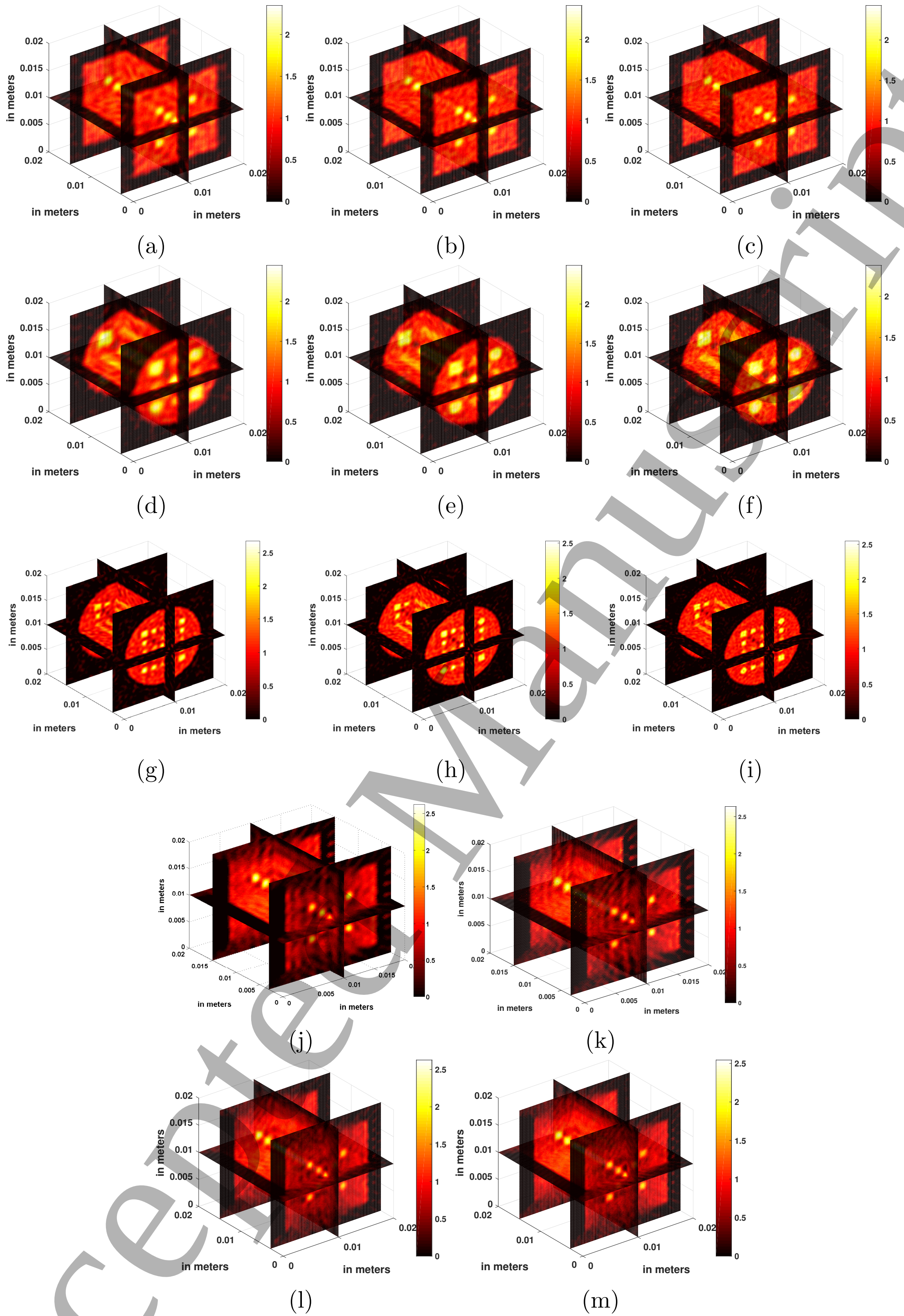

Figure 21: 3D visualization of appropriate frequency-rectangular window reconstructions. Simulation 1: **P1** using PA data with (a) 5dB SNR and $k_c = 1.0$ MHz (b)10dB SNR and $k_c = 1.4$ MHz (c) 15dB SNR and $k_c = 1.8$ MHz; **P2** using PA data with (d) 5dB SNR and $k_c = 1.0$ MHz (e) 10dB SNR and $k_c = 2.8$ MHz (f)15dB SNR and $k_c = 2.1$ MHz. Simulation 2: **P3** using PA data with (g)5dB SNR and $k_c = 1.8$ MHz (h)10dB SNR and $k_c = 2.2$ MHz (i) 15dB SNR and $k_c = 2.6$ MHz. Simulation 3A: **P1** using PA data with (g)5dB SNR and $k_c = 1.5$ MHz (h) 10dB SNR and $k_c = 1.8$ MHz. Simulation 3B: **P1** using PA data with (i)5dB SNR and $k_c = 1.5$ MHz (j) 10dB SNR and $k_c = 1.8$ MHz

6. Summary

An error estimate with respect to the band-limited reconstruction ($p_{0_{RW}}^{rec}(\vec{r})$), for UBP based PAT for arbitrary detection geometry has been reported in this study (27). In our work we have utilized a bank of filters to develop a scheme for noisy data discrimination and choosing an appropriate cut-off frequency. Numerical validations have been carried out for various phantoms of differing sizes, noise-levels and for spherical as well as planar detection geometries.

The proposed error estimate involves the cut-off frequency k_c, Laplacian of the band-limited reconstruction $\bigtriangledown^2 p_{0_{RW}}^{rec}(\vec{r})$ and double derivative of the chosen window function at the Fourier space origin $W''(0)$. The calculated error in PA reconstruction of a phantom over different filter functions with same cut-off frequency, shows proportionality with $W''(0)$ (figure 4). The proportionality of averaged error $\bar{\epsilon}$ with $W''(0)$ holds good for noisy signals as well, but the ordering of the slopes of $\bar{\epsilon}$ vs $W''(0)$ changes due to noise artifacts in reconstructions.

Observing this change of slope ordering due to noise in data, we can choose a data set with the best SNR. Such a requirement arises in practice in situations such as where sets of PA forward data of the same object have been generated under different experimental and environmental conditions. Different conditions will lead to different PA forward data. Now if we carry out the reconstructions using different filters for the datasets at different cut-off frequencies and plot the averaged error $\bar{\epsilon}$ with $W''(0)$, we can choose the signal with the best SNR on the basis of the strategy proposed in section 5.

Further, we have proposed a method to obtain an appropriate cut-off frequency k_c^a, which results in removal of noise significantly, while preserving the important features of the phantom. This is important since filtering of PA signals for attenuation of noise is accompanied by the loss of data as a trade-off. A smaller cut off window chosen for reconstruction results in loss of information about sharp boundaries and fast variations, which are reflected in the higher frequencies; while reconstructions carried out with larger cut off windows incorporate noise artifacts. The presented scheme and results obtained are essential baseline studies towards analytical reconstruction design corresponding to noisy data with known frequency domain truncations.

Acknowledgment

P.K.P. acknowledges the support of CSIR, India for his PhD scholarship during part of the work.

The authors would like to thank the referees for sharing their detailed insight which has helped in improving the manuscript.

References

[1] Wang L V and Wu H I 2007 *Biomedical Optics: Principles and Imaging, 1st ed.* (U.S.A.: Wiley-Interscience)

[2] Li C and Wang L V 2009 Photoacoustic tomography and sensing in biomedicine *Physics in medicine and biology* **54** R59

[3] Xia J, Yao J and Wang L H V 2014 Photoacoustic tomography: Principles and advances *Progress In Electromagnetics Research* **147** 1–22

[4] Wang L V and Hu S 2012 Photoacoustic tomography: in vivo imaging from organelles to organs *Science* **335** 1458–1462

[5] Maswadi S M, Ibey B L, Roth C C, Tsyboulski D A, Beier H T, Glickman R D and Oraevsky A A 2016 All-optical optoacoustic microscopy based on probe beam deflection technique *Photoacoustics* **4** 91–101

[6] Landa F J O, Deán-Ben X L, Sroka R and Razansky D 2017 Volumetric optoacoustic temperature mapping in photothermal therapy *Scientific Reports* **7** 9695

[7] Kirillin M, Perekatova V, Turchin I and Subochev P 2017 Fluence compensation in raster-scan optoacoustic angiography *Photoacoustics* **8** 59–67

[8] Joseph J, Tomaszewski M, Quiros-Gonzalez I, Weber J, Brunker J and Bohndiek S E 2017 Evaluation of precision in optoacoustic tomography for preclinical imaging in living subjects *Journal of Nuclear Medicine* jnumed–116

[9] Xu M and Wang L V 2005 Universal back-projection algorithm for photoacoustic computed tomography *Physical Review E* **71** 016706

[10] Burgholzer P, Bauer-Marschallinger J, Grün H, Haltmeier M and Paltauf G 2007 Temporal back-projection algorithms for photoacoustic tomography with integrating line detectors *Inverse Problems* **23** S65

[11] Treeby B E, Zhang E Z and Cox B 2010 Photoacoustic tomography in absorbing acoustic media using time reversal *Inverse Problems* **26** 115003

[12] Hristova Y, Kuchment P and Nguyen L 2008 Reconstruction and time reversal in thermoacoustic tomography in acoustically homogeneous and inhomogeneous media *Inverse Problems* **24** 055006

[13] Hristova Y 2009 Time reversal in thermoacoustic tomographyan error estimate *Inverse Problems* **25** 055008

[14] Sheng Q, Wang K, Matthews T P, Xia J, Zhu L, Wang L V and Anastasio M A 2015 A constrained variable projection reconstruction method for photoacoustic computed tomography without accurate knowledge of transducer responses *IEEE transactions on medical imaging* **34** 2443–2458

[15] Ding L, Ben X L D and Razansky D 2017 Efficient three-dimensional model-based reconstruction scheme for arbitrary optoacoustic acquisition geometries *IEEE Transactions on Medical Imaging*

[16] Arridge S R, Betcke M M, Cox B T, Lucka F and Treeby B E 2016 On the adjoint operator in photoacoustic tomography *Inverse Problems* **32** 115012

[17] Wang Y, Guo Z, Wang L V, Erpelding T N, Jankovic L, Robert J L and David G 2012 In vivo three-dimensional photoacoustic imaging based on a clinical matrix array ultrasound probe *Journal of Biomedical Optics* **17** 061208

[18] Laufer J G, Zhang E Z, Treeby B E, Cox B T, Beard P C, Johnson P and Pedley B 2012 In vivo preclinical photoacoustic imaging of tumor vasculature development and therapy *Journal of biomedical optics* **17** 056016

[19] Zhou Y, Li G, Zhu L, Li C, Cornelius L A and Wang L V 2015 Handheld photoacoustic probe to detect both melanoma depth and volume at high speed in vivo *Journal of biophotonics* **8** 961–967

[20] Jathoul A P, Laufer J, Ogunlade O, Treeby B, Cox B, Zhang E, Johnson P, Pizzey A R, Philip B, Marafioti T *et al.* 2015 Deep in vivo photoacoustic imaging of mammalian tissues using a tyrosinase-based genetic reporter *Nature Photonics* **9** 239

[21] Upputuri P K and Pramanik M 2016 Recent advances toward preclinical and clinical translation of photoacoustic tomography: a review *Journal of Biomedical Optics* **22** 041006

[22] Kruger R A, Kuzmiak C M, Lam R B, Reinecke D R, Del Rio S P and Steed D 2013 Dedicated 3d photoacoustic breast imaging *Medical physics* **40**

[23] Fehm T F, Deán-Ben X L, Ford S J and Razansky D 2016 In vivo whole-body optoacoustic scanner with real-time volumetric imaging capacity *Optica* **3** 1153–1159

[24] Buehler A, Herzog E, Razansky D and Ntziachristos V 2010 Video rate optoacoustic tomography of mouse kidney perfusion *Optics letters* **35** 2475–2477

[25] Xia J, Chatni M R, Maslov K I, Guo Z, Wang K, Anastasio M A and Wang L V 2012 Whole-body ring-shaped confocal photoacoustic computed tomography of small animals in vivo *Journal of biomedical optics* **17** 050506

[26] Li L, Zhu L, Ma C, Lin L, Yao J, Wang L, Maslov K, Zhang R, Chen W, Shi J *et al.* 2017 Single-impulse panoramic photoacoustic computed tomography of small-animal whole-body dynamics at high spatiotemporal resolution *Nature biomedical engineering* **1** 0071

[27] Deán-Ben X L, Razansky D and Ntziachristos V 2011 The effects of acoustic attenuation in optoacoustic signals *Physics in medicine and biology* **56** 6129

[28] Pandey P K, Naik N, Munshi P and Pradhan A 2015 Error estimates for universal back-projection-based photoacoustic tomography *European Conferences on Biomedical Optics* (International Society for Optics and Photonics) pp 953918–953918

[29] Pandey P K, Naik N, Munshi P, Pradhan A *et al.* 2016 Performance of error estimates on noisy photoacoustic data for universal backprojection based photoacoustic tomography *International Conference on Fibre Optics and Photonics* (Optical Society of America) pp W2B–4

[30] Xu M and Wang L V 2003 Analytic explanation of spatial resolution related to bandwidth and detector aperture size in thermoacoustic or photoacoustic reconstruction *Physical Review E* **67** 056605

[31] Ku G, Wang X, Stoica G and Wang L V 2004 Multiple-bandwidth photoacoustic tomography *Physics in medicine and biology* **49** 1329

[32] Dong B, Sun C and Zhang H F 2017 Optical detection of ultrasound in photoacoustic imaging *IEEE Transactions on Biomedical Engineering* **64** 4–15

[33] Huang B, Xia J, Maslov K and Wang L V 2013 Improving limited-view photoacoustic tomography with an acoustic reflector *Journal of biomedical optics* **18** 110505–110505

[34] Haltmeier M and Nguyen L V 2017 Analysis of iterative methods in photoacoustic tomography with variable sound speed *SIAM Journal on Imaging Sciences* **10** 751–781

[35] Mitsuhashi K, Wang K and Anastasio M A 2014 Investigation of the far-field approximation for modeling a transducer's spatial impulse response in photoacoustic computed tomography *Photoacoustics* **2** 21–32

[36] Fehm T F, Deán-Ben X L and Razansky D 2014 Four dimensional hybrid ultrasound and optoacoustic imaging via passive element optical excitation in a hand-held probe *Applied Physics Letters* **105** 173505

[37] Natterer F 1986 *The mathematics of computerized tomography* vol 32 (Siam)

[38] Herman G T 2009 *Fundamentals of computerized tomography: image reconstruction from projections* (Springer Science & Business Media)

[39] Munshi P, Rathore R, Ram K and Kalra M 1991 Error estimates for tomographic inversion *Inverse Problems* **7** 399

[40] Wells P, Fillingham N and Cramond A 1996 A study of errors due to reconstruction filters in computed tomography *Journal of Research in Nondestructive Evaluation* **8** 149–163

[41] Jain N, Kalra M and Munshi P 2011 Characteristic signature of specimen using an approximate formula for 3d circular cone-beam tomography *Research in Nondestructive Evaluation* **22** 169–195

[42] Athe P, Shakya S, Munshi P, Luke A and Mewes D 2013 Characterization of multiphase flow in bubble columns using kt-1 signature and fractal dimension *Flow Measurement and*

Instrumentation **33** 122–137

[43] Shakya S, Munshi P, Behling M, Luke A and Mewes D 2014 Analysis of dynamic bias error in x-ray tomographic reconstructions of a three-phase flow system *International Journal of Multiphase Flow* **58** 57–71

[44] Shakya S, Munshi P, Luke A and Mewes D 2015 Computerized tomography application in oil industry using kt-2 signature *Research in Nondestructive Evaluation* **26** 61–89

[45] Strauss W A 1992 *Partial differential equations* vol 92 (Wiley New York)

[46] Dray T and Manogue C A 2010 book:math:delta3d — the geometry of vector calculus [Online; accessed 3-February-2017] URL http://math.oregonstate.edu/BridgeBook/doku.php?id=book:math:delta3d&rev=1277055518

[47] Treeby B E and Cox B T 2010 k-wave: Matlab toolbox for the simulation and reconstruction of photoacoustic wave fields *Journal of biomedical optics* **15** 021314–021314

[48] Munshi P, Rathore R, Ram K S and Kalra M 1993 Error analysis of tomographic filters ii: results *NDT & E International* **26** 235–240

[49] Press W H, Teukolsky S A, Vetterling W T and Flannery B P 1996 *Numerical recipes in C* vol 2 (Cambridge university press Cambridge)

[50] Klose A 2002 *Optical tomography based on the equation of radiative transfer* Ph.D. thesis Freie Universität Berlin